

# Natural Fractal Structures

## ...to the microscopic

This chapter will discuss fractal structures encountered in the physics of condensed matter and solids, that is, disordered media, thin evaporated films, porous media, diffused structures, colloids and aerosols, aggregates, deposited layers, polymers, and membranes. Aside from the interest arising from the description and understanding of the physical processes generating such peculiar structures, knowledge of the geometry of these structures may have important consequences in various technological fields: microelectronics, for disordered materials and thin or deposited films; petroleum recovery, for porous materials; gelification and rheological properties for polymers, etc. As in Chap. 2, physical phenomena of the same type (of the same universality class) will also be discussed.

### 3.1 Disordered media

Disordered media is the term used to denote media composed of a random agglomeration of at least two types of material. Examples include alloys, discontinuous deposits of metallic films, diluted magnetic materials, polymer gels, and general composite materials. This section will present percolation as a theoretical model, and describe experimental studies on evaporated films which, due to their two-dimensional nature, lend themselves to analysis. The study of other disordered materials such as alloys or composites is found in Chap. 5 on transport in heterogeneous media.

#### 3.1.1 A model: percolation

Percolation plays a fundamental role in a considerable number of physical phenomena in which disorder is present within the medium. Examples include: heterogeneous conductors, diffusion in disordered media, forest fires, etc. In Table I below, extracted from Zallen (1983), we give a partial list of its applications. Here we can see the extent of the range of applications of

TABLE I: Areas of application of percolation theory

Phenomenon or system	Transition
Random star formation in spiral galaxies	: Nonpropagation / Propagation
Spread of a disease among a population	: Contagion contained/ Epidemic
Communications network or resistor network	: Disconnected / Connected
Variable distance jump (amorphous semiconductors)	: Analoguous to resistors networks
Flow of a liquid in a porous medium	: Localized / Extensive wetting
Composite materials, conductor – insulator	: Insulator / Metal
Discontinuous metallic films	: Insulator / Metal
Dispersion of metallic atoms in conductors	: Insulator / Metal
Composite materials, superconductor – metal	: Metal / Superconductor
Thin films of helium on surfaces	: Normal / Superfluid
Diluted magnetic materials	: Para / Ferromagnetic
Polymer gels, vulcanization	: Liquid / Gel
Glass transition	: Liquid / Glass
Mobility threshold in amorphous semiconductors	: Localized / Extended states
Quarks in nuclear matter	: Confinement / Nonconfinement

percolation; like fractal structures themselves, percolation is found in models of galaxy formation as well as in the distribution of quarks in nuclear matter. The table reveals that the physical systems involved all undergo transitions. Within the framework of percolation, this transition is related to a phase transition. Indeed, the close parallel between percolation and phase transition is mathematically demonstrable.

Many experiments bring to light the characteristics of percolation. We shall describe a certain number in this section, but more will appear elsewhere in this book during discussion of other topics.

### ***What is percolation?***

Percolation was introduced in an article published by Broadbent and Hammersley in 1957. The word “percolation” originated from an analogy with a fluid (the water) crossing a porous medium (the coffee). As it transpires, the invasion of a porous medium by a fluid is in fact more complex (see Sec. 3.2) than the theoretical model that we are going to present now.

By way of a simple introduction to percolation, imagine a large American city whose streets form a grid (square network) and a wanted person, “Ariane”, who wishes to cross the city from East to West (Fig. 3.1.1). Now, the police in this city are badly trained, choosing to set up roadblocks in the streets merely at random. If  $p_B$  is the proportion of streets remaining open, the probability of Ariane crossing the city decreases with  $p_B$ , and the police notice

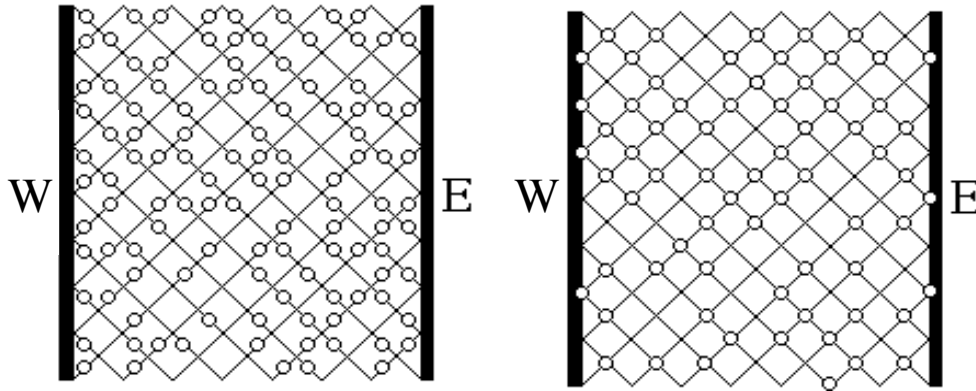


Fig. 3.1.1. On the left, bond percolation: out of 224 bonds, 113 are broken (white points), however there is still a route from East to West. On the right, site percolation: out of 128 sites, 69 are blocked, but there is no route through in this example.

(the city is very large) that with  $p_B = p_{B_c} = 1/2$  they are almost certain (in the probabilistic sense) of stopping Ariane. The problem that we have just devised is one of bond percolation (the streets which form the bonds between crossroads are forbidden). The concentration  $p_{B_c}$  is called the bond percolation threshold.

For this result the city must be very large, as this threshold,  $p_{B_c}$ , is in fact a limit as the size (of the city, network, etc.) tends towards infinity. We shall return to the subject of the effects of finite size later.

But let us return to Ariane as, after some thought, the police, although continuing to set up roadblocks at random, have now decided to place them at crossroads. They now notice that the number of roadblocks required is smaller. There are two reasons for this: first, the number of crossroads is half that of the streets (if the city is large enough to ignore the outskirts), and second, if  $p_S$  is the proportion of crossroads remaining empty, we find a percolation threshold  $p_{S_c} = 0.5927\dots$ , i.e. it is sufficient to control about 41% of the crossroads. This is a case of site percolation (since in a crystalline network the “crossroads” are the sites occupied by the atoms).

If our network of streets is replaced by a resistor network some of which are cut, the current passing between W and E as a function of the proportion of resistors left intact is given by the graph below (Fig. 3.1.2). The current is zero for  $p < p_c$ , while, over the percolation threshold  $p_c$  it increases. We shall study this in greater detail in Sec. 5.2, which focuses on transport phenomena.

To summarize, we can say that the percolation threshold corresponds to the concentration (of closed bonds, etc.) at which a connected component of infinite extent appears (or disappears): a path is formed and, in materials where connected components conduct, the current flows. We can now begin to see why transitions were mentioned in the table shown at the start of the section.

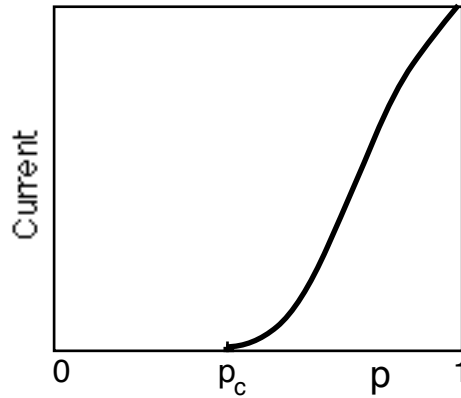


Fig. 3.1.2. Variation in the current passing between two opposite faces of a network of resistors of which a proportion  $(1-p)$  are cut at random. There is a threshold  $p_c$  of intact resistors such that a path allowing current to flow can be found. This threshold is better defined the larger the network.

The graph shown in Figure 3.1.2 could also represent, say, the conductivity of a random distribution of insulating and conducting balls ( $p_c$  is then about 0.3).

### Percolation over regular networks

The first studies on percolation were for regular networks (relating to crystalline structures, which are mathematically simpler). Here we shall outline some properties and define various substructures which will of use further on. For a more precise and mathematical treatment consult Essam, 1972 & 1980 and Stauffer, 1985.

Except in certain two-dimensional networks (indicated by an asterisk in Table II), where, by symmetry,  $p_c$  can be calculated exactly, the percolation threshold can only be found by numerical simulation or by series extrapolation (Table II). The method employed in calculating the percolation threshold by

Table II: Percolation thresholds for some common networks

$p_c$	Site ( $p_{sc}$ )	Bond ( $p_{bc}$ )
Honeycomb	0.6962	0.65271*
Square	0.59275	0.50000
Triangular	0.50000*	0.34719
Diamond	0.428	0.388
Simple cubic	0.3117	0.1492
Base centered cubic	0.245	0.1785
Face centered cubic	0.198	0.199

numerical simulation consists in finding the concentration at which a

percolation cluster appears in a network of size  $L^d$ , and then extrapolating the results as  $L \rightarrow \infty$ . This method is not very precise in practice, and, with enough memory and computer time, more elaborate calculational techniques on stripes or concentration gradients are preferable. Calculating the threshold by series extrapolation involves analytically determining the probabilities of occurrence of as many as possible finite cluster configurations [see for instance the calculation of  $P_\infty(p)$ , Eq. (3.1-4), where the clusters used in the calculation are only the very smallest ones], and then trying to extrapolate to very large clusters. Note that in two-dimensions there are duality transformations between networks (e.g., the transformation star  $\leftrightarrow$  triangle) which induce relationships between their respective thresholds, thus enabling exact calculations to be made in certain cases.

In the case of a *Cayley tree*, in which each site has  $z$  first neighbors (also known as a Bethe network), the exact solution may also be found:  $p_c = 1/(z-1)$  (see below for the mean field approach). In Fig. 3.1.3, a part of a Cayley tree is shown with  $z = 3$ :

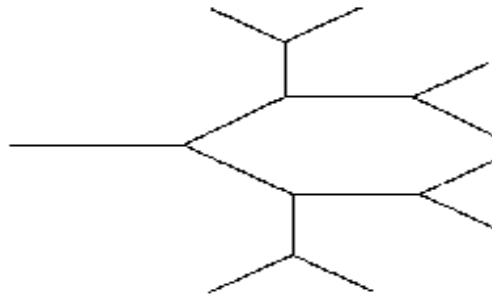


Fig. 3.1.3. Part of a Cayley tree with  $z = 3$  branches attached to each site (the network continues indefinitely, of course, along all of its branches).

### **Subset of occupied sites**

Below the threshold, the percolation network is composed solely of finite clusters, a cluster being defined as a set of connected sites or bonds. If  $s$  is the size of a finite cluster (on the diagram below two finite clusters have been indicated:  $s = 1$  and  $s = 4$ ) and if  $n_s$  is the number of clusters of size  $s$  per site,  $sn_s$  is the probability of finding a given site belonging to a cluster of size  $s$ . Since below the threshold an occupied site is necessarily in a finite cluster, the probability of a site being occupied leads to the relation

$$\sum_s s n_s = p.$$

As the concentration reaches the percolation threshold, i.e., when  $p \geq p_c$  ( $\cong 0.59$  for a square lattice), an *infinite cluster*, or *percolation cluster*, appears (shaded gray in Fig. 3.1.4). At the threshold itself, the probability,  $P_\infty$ , of a

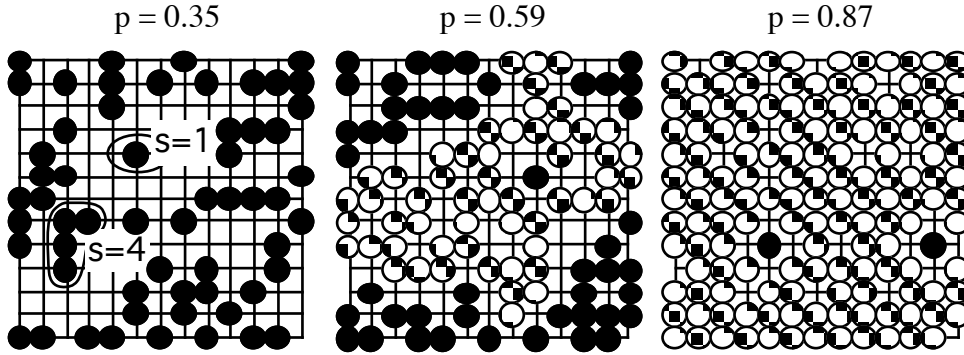


Fig. 3.1.4. Square network ( $L \times L$ ,  $L = 13$ ) for three concentrations,  $p$ , of occupied sites. For sufficiently small  $p$  there are only finite clusters ( $s = 1, \dots, 4, \dots$ ). At a certain concentration  $p_c(L)$ , a percolation cluster (shaded grey) emerges. At higher concentrations this cluster invades the network. As  $L \rightarrow \infty$ ,  $p_c(L) \rightarrow p_c$  and the percolation cluster becomes an infinite fractal cluster.

site to belong to this cluster is still zero. This infinite cluster which emerges at the percolation threshold is often called the *incipient infinite cluster*. Above the threshold, the probability  $P_\infty$  grows very rapidly. An occupied site is now either in a finite cluster or in the infinite cluster, and hence

$$P_\infty + \sum_s s n_s = p \quad (3.1-1)$$

In the neighborhood of  $p_c$  the function  $P_\infty(p)$  behaves as

$$P_\infty(p) \propto (p - p_c)^\beta \quad (3.1-2)$$

with  $\beta = 5/36$  for two-dimensional networks ( $d = 2$ )  
 and  $\beta \cong 0.44$  for three-dimensional networks ( $d = 3$ ).

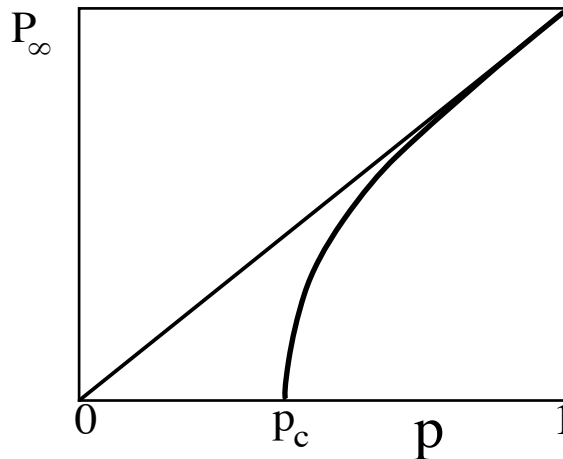


Fig. 3.1.5. Probability of a site being in the infinite cluster. Away from the threshold, when nearly all the sites belong to this cluster,  $P_\infty$  varies like  $p$ .

We shall frequently observe this kind of behavior on the part of physical quantities. The exponents (here denoted  $\beta$ ) are numbers which, generally speaking, depend only on the model being studied (in this case, percolation) and the Euclidean dimension  $d$  of the space. They are, for example, independent of the shape of the network (square, triangular, or honeycomb). In particular,  $\beta$  is the same for site and bond percolation. There is said to be *universality* present. This characteristic is also found in the case of phase transitions close to the critical temperature  $T_c$ , including magnetism close to the Curie temperature.

Some of these exponents represent *fractal dimensions*, although the *mathematical* reasons are as yet unknown.

**Calculating  $P_\infty(p)$**

We can, in theory, calculate the probability  $P_\infty(p)$  arithmetically by considering the following equation<sup>1</sup>

$$P_\infty(p) = 1 - P_{\text{finite}}(p) \tag{3.1-3}$$

and calculating  $P_{\text{finite}}(p) = \sum_{s=0}^\infty P_s(p)$ , where  $P_s$  is the probability for a site to belong to a cluster of size  $s$ . For site percolation over a square network (an empty site is represented by a white disk, an occupied site by a black disk), we have, for example,

$$\begin{array}{lll}
 P_0 = & \text{○} & = q \equiv 1 - p \\
 \\
 P_1 = & \begin{array}{c} \text{○} \\ \text{○} \bullet \text{○} \\ \text{○} \end{array} & = p q^4 \\
 \\
 P_2 = & \begin{array}{c} \text{○} \\ \text{○} \bullet \text{○} \\ \text{○} \bullet \text{○} \\ \text{○} \end{array} & = 2 \times 4 p^2 q^6
 \end{array}$$

... and in general ( $s > 0$ ),

$$P_s = s n_s = \sum_t g_{st} p^s q^t, \tag{3.1-4}$$

where  $t$  is the size of the perimeter of the cluster, i.e., the set of empty sites which are first neighbors to one of the sites of the cluster. The difficulty, of course, is in calculating  $g_{st}$ : no expression is known for large  $s$ , and yet all the properties of percolation arise from the statistics of large clusters. Series of this type have been studied extensively, especially when the first detailed work on percolation was being carried out (de Gennes et al., 1959; Essam, Sykes, and

---

<sup>1</sup> The probability of being in either a finite ( $s \geq 0$ ) or infinite cluster is 1.

Essam: see Essam, 1980). They provided the first values of  $p_c$ , the critical exponents, etc.

### Mean field approach

Failing a rigorous method of determining the probability  $P_\infty(p)$ , an approach based on a *mean field* (also known as an *effective field*) calculation has been tried. The first studies of this kind are due to Flory and Stockmayer (see Flory, 1971) who, in as early as 1941, were investigating the appearance of gelification in polymers by developing a mean field approach over a Bethe network, before the idea of percolation had even emerged (we shall discuss this again later in Sec. 3.5 on gels).

Mean field calculations work as follows: taking Fig. 3.1.6(a) as our starting point, we see that for site **a** to belong to a finite cluster it must either be an empty cluster, with probability  $1-p$ , or be occupied, with probability  $p$ , and then connected to a finite cluster by one of its  $z$  neighbors. So we can now write

$$P_{\text{finite}}(p) = (1-p) + p G^z, \quad (3.1-5)$$

where  $G$  is the probability that a site neighboring **a** belongs to a finite cluster ( $0 \leq G \leq 1$ ). In this equation we must assume independence between the branches (no loops).

Taking one of these  $z$  neighbors, we see that it is itself linked to  $(z-1)$  second neighbors and so we have,

$$G(p) = (1-p) + p G^{z-1}. \quad (3.1-6)$$

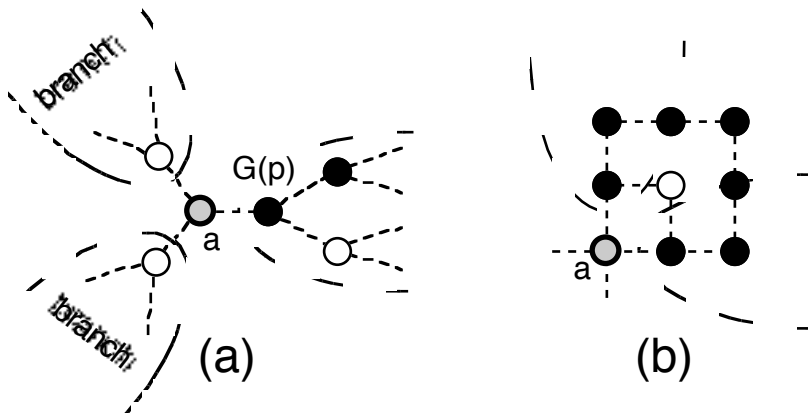


Fig. 3.1.6. (a) Diagram showing mean field approximation. Site **a** of a finite cluster may either be occupied or empty; if it is occupied it must have each of its  $z$  ( $= 3$ ) neighboring sites belonging to a finite cluster, which they each do with probability  $G$ . These sites must in turn either be empty or connected to one of the  $z-1$  second neighbor sites, again belonging to finite clusters with probability  $G$ . (b) This approach is only approximate if there are loops linking the branches.

This approach does in fact completely resolve the problem of percolation over a Bethe network (which has no loops).

i) For  $z = 2$ , the network is a linear chain; so Eq. (3.1-6) is now

$$G = 1 - p + pG. \quad (3.1-6a)$$

Hence, when  $p \neq 1$ , Eq. (3.1-6a) has as its solution  $G \equiv 1$ , and so [from (3.1-5)]:  $P_\infty \equiv 0$ . When  $p = 1$ ,  $G$  is not determined by Eq. (3.1-6a), but as all the sites of the chain are occupied,  $P_\infty = 1$  and the percolation threshold occurs at  $p_c = 1$ .

ii) For  $z = 3$ , the network is hexagonal (or honeycomb); So Eq. (3.1-6) now becomes:

$$G = 1 - p + pG^2. \quad (3.1-6b)$$

This equation possesses two roots:  $G = 1$  and  $G = (1-p)/p$ . The solution  $G = (1-p)/p$  is only valid for  $p \geq p_c = 1/2$ , as we require  $0 \leq G \leq 1$ , and in this case it may be shown that  $G = 1$  is not a valid solution. Hence,

(a) when  $p < p_c = 1/2$ , there is only one solution:  $G = 1$  and  $P_\infty = 0$ ,

(b) when  $p > p_c = 1/2$ ,  $G = (1-p)/p$  is the unique solution and an *infinite cluster* occurs, with the probability of a site belonging to it given by

$$P_\infty = p - q^3/p^2.$$

In the neighborhood of  $p_c$  ( $p = 1/2 + \epsilon$ ) we find:

$$G \cong 1 - 4\epsilon \quad \text{hence} \quad P_\infty(p) \cong 6\epsilon = 6(p - p_c).$$

iii) Similarly, it can be shown for any value of  $z$  that

$$P_\infty(p) = 2z/(z-2) (p - 1/(z-1))^\beta + \dots \quad \text{with } \beta = 1. \quad (3.1-7)$$

Thus, a *mean field* approach yields  $\beta = 1$ .

Eqs. (3.1-5) and (3.1-6) provide exact results for Bethe networks, hence much interest has been shown in this type of network. They represent textbook examples of mean field approaches to percolation problems.

It is interesting to compare the first iterations in mean field calculations with those of an exact calculation. Thus for  $z = 4$  (square network), although we find the beginning of the series for  $P_{\text{finite}}$  to be the same up to clusters of size two, from there they differ. In mean field,

$$P_{\text{finite}}(p) = q + p q^4 + 2 \times 4 p^2 q^6 + 3 \times 18 p^3 q^8 + 4 \times 88 p^4 q^{10} + \dots, \quad (3.1-8a)$$

whereas the exact calculation gives,

$$P_{\text{finite}}(p) = q + p q^4 + 2 \times 4 p^2 q^6 + 3 \times (12 p^3 q^7 + 6 p^3 q^8) + 4 \times (36 p^4 q^8 + 32 p^4 q^{10} + 8 p^4 q^{10}) + \dots \quad (3.1-8b)$$

The two series differ as soon as loops are possible, or to be more precise, as soon as sites on the perimeter have several first neighbors in the cluster (loops including a perimeter site; this occurs for clusters of size 3).

***Summary of three things to remember***

(1) The mean field approach is equivalent to solving for a Bethe network, that is, a network in which loops never occur. It is the loops which make the problem insoluble at present by introducing correlations between the probabilities.

(2) The mean field approach provides a set of critical exponents which may be completely determined. We have calculated  $\beta$  ( $= 1$ ) here. The mean field exponents are themselves *universal*. Their values are shown in the table at the end of the section under the heading “Bethe”.

(3) The dimension at which the mean field becomes exact is called the *critical dimension*, which is when the probability of loops forming is zero. If the dimension of the space is increased, the room available for branches in a percolation cluster grows sufficiently large to make the occurrence of loops very rare (i.e., of probability going to zero as the size of the incipient infinite cluster goes to infinity). Consequently, for all dimensions  $d \geq d_c$ , the mean field becomes exact. This dimension is mainly of theoretical interest [because it can be expanded in the neighborhood of  $d_c$ : ( $d = d_c - \epsilon$ ) it can be compared with other methods]. In the case of percolation, the critical dimension  $d_c = 6$  (and the fractal dimension of the infinite cluster is then  $D = 4$ , see below).

Besides  $P_\infty(p)$ , there are other quantities of great physical significance.

These include:

- $S(p)$ : the mean number of sites in a finite cluster (Fig. 3.1.7).
- $\xi(p)$ : the connection length, mean radius of the finite clusters.

To these we might add:

- $\Sigma(p)$ : the mean macroscopic conductivity in metal–conductor mixtures, about which we shall only say a few words in this section.

The mean size of the finite clusters, i.e., the mean number of sites contained in one of them,  $S(p)$ , diverges at  $p_c$  because of the emergence of an infinite cluster. By definition,

$$S(p) = \langle s \rangle = \sum_s s(sn_s) / \sum_s sn_s = \sum s^2 n_s / p. \quad (3.1-9)$$

It behaves as

$$S(p) \propto |p - p_c|^{-\gamma} \quad (3.1-10)$$

where  $\gamma = 43/18$  when  $d = 2$ .  
 $\gamma \cong 1.8$  when  $d = 3$ .

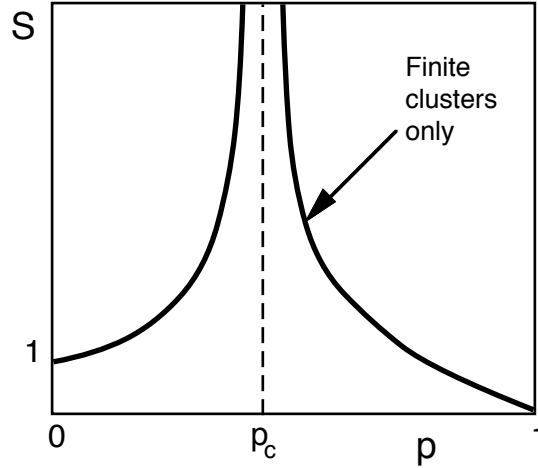


Fig. 3.1.7. Mean size of finite percolation clusters.  $S(p)$ 's behavior is governed by the same exponent above and below the threshold.

Remark: When  $p > p_c$  the infinite cluster is, of course, not taken into account in the calculation of  $S(p)$ .

### Cluster radius and fractal dimension

A cluster of size  $s$  has a certain mean radius  $R_s$ . In practice, it is useful to define it by what is known as the *radius of gyration*, that is, the radius at which all the “mass” would need to be situated for there to be an equal moment of inertia. We let

$$R_s^2 = \frac{1}{s} \sum_{i=1}^s |\vec{r}_i - \vec{r}_0|^2, \quad (3.1-11a)$$

where  $\vec{r}_0 = \frac{1}{s} \sum_{i=1}^s \vec{r}_i$  (center of mass),  $i$  being a site of the cluster.

This may also be written

$$R_s^2 = \frac{1}{2s^2} \sum_{i,j} |\vec{r}_i - \vec{r}_j|^2. \quad (3.1-11b)$$

The correlation (or, better here, connection) length  $\xi(p)$  is the mean radius of gyration of *all* the finite clusters. It gives an idea of the average distance at which the connectivity makes itself felt. Since there is a probability  $sn_s$  of a randomly chosen site,  $i$ , belonging to a cluster of size  $s$ , and there are  $s$  sites  $j$  corresponding to such a site, we define  $\xi^2$  by the relation

$$\xi^2(p) = \langle R_s^2 \rangle = \frac{2 \sum_s R_s^2 s^2 n_s}{\sum_s s^2 n_s}. \quad (3.1-12)$$

As  $p$  approaches  $p_c$  from below, an infinite cluster emerges, that is, one of infinite radius of gyration. Thus,  $\xi$  must diverge at  $p_c$ . When  $p > p_c$ ,  $\xi$  is still

defined as the average over finite clusters; it diverges as  $p$  tends to  $p_c$  from above. As with the other quantities described earlier,  $\xi$  behaves according to a power law close to  $p_c$ . We may thus write (the notation  $\nu$  is adopted for the critical behavior of the correlation length whatever the type of model)

$$\xi(p) \propto |p - p_c|^{-\nu} . \quad (3.1-13)$$

The exponent  $\nu$  is the same on either side of  $p_c$ . The values of  $\nu$  are

$$\nu = 4/3 \text{ when } d=2; \quad \nu \cong 0.88\dots \text{ when } d=3.$$

This correlation length is directly related to the correlation function,  $g(r)$ , the probability that a site at distance  $r$  from an occupied site belongs to the *same finite cluster* [ $g(0)$  is normalized to one].

$$g(r) = \frac{\langle m(\vec{r}_0) m(\vec{r}_0 + \vec{r}) \rangle}{\langle m(\vec{r}_0) \rangle} = \langle m(\vec{r}_0) m(\vec{r}_0 + \vec{r}) \rangle / p . \quad (3.1-14)$$

As the only contributions to  $g(r)$  come from occupied sites  $r_0$  and  $r_0+r$ , [ $m(r_0) = m(r_0+r) = 1$ ], the average number of sites to which an occupied site  $r_0$  is connected is  $p \sum_r g(r)$ , the summation ranging over all the sites of the network. This mean number is therefore  $\sum_s s^2 n_s$ , so that

$$p S(p) = \sum_s s^2 n_s = p \sum_r g(r) . \quad (3.1-15)$$

The mean distance  $\xi$  is the weighted sum of the mean distances between two sites belonging to the same cluster, so we have

$$\xi^2 = \sum_r r^2 g(r) / \sum_r g(r) . \quad (3.1-16)$$

The relation (3.1-13) enables us to evaluate the effects of finite size on the value of the percolation threshold. Indeed, for a sample of size  $L$ , the concentration at which the finite clusters percolate is on average such that  $\xi(p) \cong L$ . The apparent threshold is therefore

$$p_c^* \cong p_c - C L^{-1/\nu} . \quad (3.1-17)$$

### **Fractal dimension**

By calculating quantities such as  $R_s$  or  $g(r)$ , various relationships may be found concerning the distribution of occupied sites in a finite cluster, in the case of  $R_s$ , and their mean distribution, in the case of  $g(r)$ . This allows the following question to be posed: are the size  $s$  and the radius  $R_s$  of a cluster related by a power law defining a fractal dimension?

Numerical experiments and phase transition considerations (renormalization group) demonstrate that this is precisely the case for large clusters at the percolation threshold. Indeed, the mass–radius relation may be written

$$s \propto R_s^D \quad (p = p_c, s \rightarrow \infty). \quad (3.1-18)$$

(At  $p = p_c$ , there exists an infinite cluster and many finite clusters whose structures merge with the infinite cluster as  $s \rightarrow \infty$ .)

This fractal structure is also obtained by averaging over all the finite clusters: if we calculate the mean mass at  $p = p_c$  of occupied sites belonging to the same finite cluster by integrating the correlation function  $g$  over an annulus between  $r$  and  $r+dr$ , we find

$$M(R) \propto \int_0^R r^{d-1} g(r) dr \propto R^D. \quad (3.1-19)$$

This forces the asymptotic behavior of  $g(r)$  to be

$$g(r) \propto \frac{1}{r^{d-D}} \quad (p = p_c). \quad (3.1-20)$$

It can be shown that  $D = 91/48 \cong 1.89$  when  $d = 2$ ,  
 $D \cong 2.5$  when  $d = 3$ .

When we no longer have  $p = p_c$ , the scaling function takes the general form

$$g(r, \xi) \propto \frac{1}{r^{d-D}} \Gamma\left(\frac{r}{\xi(p)}\right) \quad (3.1-21)$$

and the mass in a ball of radius  $R$  is

$$M(R, \xi) \propto \xi^D \Phi\left(\frac{R}{\xi(p)}\right) \quad \text{with} \quad \Phi(x) = \int_0^x u^{D-1} \Gamma(u) du \quad (3.1-22)$$

These important expressions are worth discussing further. When  $p = p_c$ ,  $\xi$  is infinite and  $g$  is a simple power law of the form (3.1-20), characteristic of a fractal distribution. But if  $p \neq p_c$ , the finite clusters have a mean radius  $\xi$  which is then the only significant distance in the system; there is of course a minimum distance  $a$  (distance between sites, for example), but when the clusters are sufficiently large this length plays no role. In general, there is also a maximum length,  $L$  (size of the sample), which is assumed here to be very large in relation to  $\xi$ . So we postulate that the ratio  $g(r, \xi)/g(r, \infty)$  is a dimensionless scaling function  $\Gamma(r/\xi)$ .<sup>2</sup> We have already encountered this sort of formulation in our treatment of Koch curves [expression (1.4-1)]. This function  $\Gamma$  is not explicitly known, but its limit values may be determined: close to  $p_c$ ,  $\Gamma(x \ll 1)$  is a nonzero constant [for Eq. (3.1-21) to be satisfied] and  $\Phi(x) \propto x^D$ ; for  $r > \xi$ ,  $\Gamma(x \gg 1)$  tends (exponentially) to zero, as there are no longer any sites in the cluster, and  $\Phi$  becomes constant.

If  $g(r)$  is calculated *over the infinite cluster* when  $p > p_c$ , an expression of

<sup>2</sup> When  $L$  is not so large finite size effects occur. In practice these are nearly always present [see, e.g., Eq. (3.1-17)].

the form (3.1-21) is obtained, since the correlation length over this cluster is determined by the clusters of empty sites distributed within it. These have a size distribution comparable to that of the finite clusters present in the medium. The difference in this case is that for  $r \gg \xi$ , the mass distribution becomes homogeneous of dimension  $d$ :  $M \propto r^d$ , so that  $\Gamma(x \gg 1) \propto x^{d-D}$ .

### ***Can any relations between the exponents be found?***

Several relations (*scaling laws*) between the critical exponents have been proved or conjectured. These relations were discovered in the 1960s and 1970s when studies on scale (or dilation) invariance were being carried out, which presaged fractal structures and the renormalization group.<sup>3</sup> We shall introduce them as they are required.

### ***Relations between $\beta$ , $\nu$ , $d$ and $D$***

Consider the distribution of occupied sites in the infinite cluster within a sphere of radius  $\xi$ . On the one hand, from above, the number of sites situated in the sphere may be calculated by taking into account its fractal nature:

$$M = \xi^D \propto (p-p_c)^{-\nu D}$$

On the other, it may be observed that this number is proportional to the product of the probability of a site being in the infinite cluster,  $P_\infty$ , and the number of (empty or occupied) sites present,  $\xi^d$ . Comparing these two calculations we find the scaling law

$$\boxed{D = d - \beta/\nu} . \quad (3.1-23)$$

This relation has been well verified numerically.

### ***Distribution of the cluster sizes***

It is also very important to know about the cluster distribution. Here again we are looking for the asymptotic behavior, that is, the distribution,  $n_s$ , of large clusters of size  $s$ . *At the percolation threshold*, because of the dilation invariance of the cluster distribution, we should expect a distribution of the form

$$n_s \propto s^{-\tau}, \quad s \rightarrow \infty. \quad (3.1-24a)$$

This behavior is also well verified numerically in those expressions where the exponent  $\tau$  appears.

When  $p = p_c$  no longer holds, the scaling function takes the general form

$$n_s \propto s^{-\tau} f(|p - p_c| s^\sigma), \quad s \rightarrow \infty. \quad (3.1-24b)$$

---

<sup>3</sup> The many authors who established the foundations of this important field are not cited here. The reader can refer to classic books.

Table III – Percolation exponents in  $d = 2, d = 3$  and for the Bethe lattice  
(Stauffer, 1985)

Exponent	$d = 2$	$d = 3$	Bethe	Quantity
$\alpha$	$-2/3$	$-0.6$	$-1$	Total number of clusters
$\beta$	$5/36$	$0.42$	$1$	Infinite cluster
$\gamma$	$43/18$	$1.8$	$1$	Mean finite cluster size
$\nu$	$4/3$	$0.88$	$1/2$	Correlation length
$\sigma$	$36/91$	$0.45$	$1/2$	Number of clusters $p = p_c$
$\tau$	$187/91$	$2.2$	$5/2$	Number of clusters $p = p_c$
$D(p = p_c)$	$91/48$	$2.52$	$4$	Fractal dimension
$D(p < p_c)^4$	$1.56$	$2.0$	$4$	Fractal dimension
$D(p > p_c)^5$	$2$	$3$	$4$	Fractal dimension
$\mu$	$1.3$	$2.0$	$3$	Conductivity

$\sigma$  may be found fairly easily. The quantity appearing in the scaling function must be dimensionless: say, of the form  $R_s/\xi$ , with  $\xi$  representing the unique scale length of the system.  $R_s$  varies as  $s^{1/D}$ , while  $\xi \propto |p-p_c|^{-\nu}$ ; as a result  $s^{1/D}|p-p_c|^\nu$  and, hence,  $s^{1/\nu D}|p-p_c|$  are invariant. Thus,

$$\sigma = 1/\nu D . \quad (3.1-25)$$

Knowing  $n_s$ , all the mean values mentioned earlier may be calculated:  $P_\infty$ ,  $S$ , etc. Using the relationship,  $P_\infty(p) + \sum_s s n_s(p) = p$ , close to  $p_c$ , and the fact that  $P_\infty(p_c) = 0$  and  $\sum_s s n_s(p_c) = p_c$ :

$$P_\infty(p) = p - p_c + \sum_s s \{n_s(p_c) - n_s(p)\} .$$

In the neighborhood of  $p_c$ ,  $P_\infty(p)$  is given by the singular part (for  $p > p_c$ ) of the expression above. We make this calculation by replacing the discrete sum with an integral: after integration by parts, taking  $\tau > 2$ ,

$$P_\infty(p) \propto \int_0^\infty (n_s(p_c) - n_s(p)) s ds = (p - p_c)^{\frac{\tau-2}{\sigma}} \int_0^\infty dz z^{2-\tau} f(z) ,$$

that is,

$$\tau = \beta\sigma + 2 . \quad (3.1-26)$$

The exponent  $\gamma$  of  $S(p)$  may also be calculated:

<sup>4</sup> This is the fractal dimension of the very large clusters whose diameter is much greater than the correlation length of the percolation. These clusters, which are much more tenuous than the incipient percolation cluster and which have long “legs,” are known as “animals.” The dimension  $D(p = p_c)$ , on the other hand, corresponds to the large clusters when  $p \equiv p_c$  whose diameter is of the order of  $\xi$ .

<sup>5</sup> This is the dimension of the infinite cluster well above the threshold. It is known to be dense at distances greater than  $\xi$  (and of course fractal at distances less than  $\xi$ ).

$$\gamma = (3 - \tau) / \sigma, \quad (3.1-27)$$

along with many other exponents. All these exponents relating to the geometric structure may be expressed in terms of any two of them ( $\nu$  and  $D$ , for example).

### ***Spreading dimension in percolation***

This dimension (cf. Sec. 1.5.1) has been estimated by numerical simulation. The first calculations were carried out by Vannimenus *et al.* (1984). The most recent values are (see Bunde and Havlin, 1991):

$$\begin{aligned} d_f &\cong 1.678 \pm 0.005, \text{ when } d=2, \\ d_f &\cong 1.885 \pm 0.015, \text{ when } d=3. \end{aligned}$$

The length of the shortest path in terms of the distance,  $L$ , as the crow flies is such that  $L_{\min} \propto L^{d_{\min}}$ , where

$$d_{\min} \cong 1.14 \text{ in } d=2 \text{ and } d_{\min} \cong 1.39 \text{ in } d=3.$$

### ***Backbone***

A very important subset is the one known as the *backbone* of the percolating cluster (Fig. 3.1.8). This is the set of connected sites available for conduction (see also Sec. 4.2). Of course, there will be a backbone only at concentrations greater than the threshold.

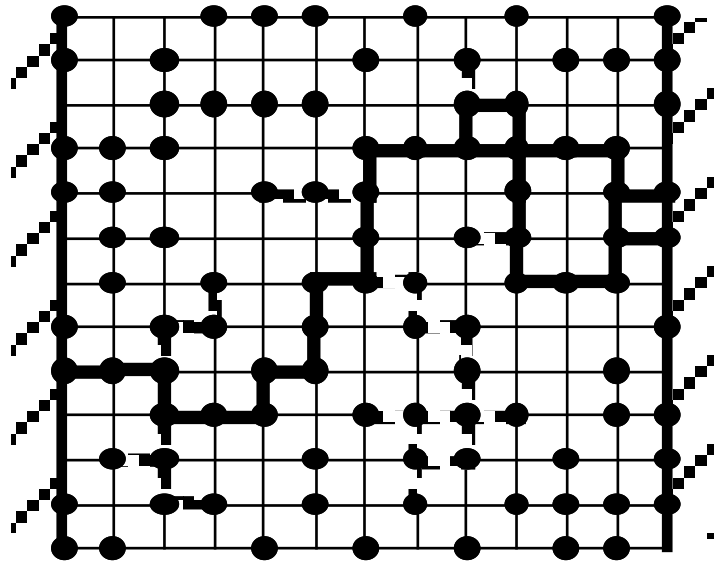


*Fig. 3.1.8. The infinite cluster (here the network is of finite size) is composed of a backbone which is a simply or multiconnected set of bonds (solid line) and of dead ends (shaded lines). These dead ends contain nearly all the mass of the percolation cluster in the limiting case of an infinite network.*

It also possesses a *fractal structure*, whose dimension is

$$\begin{aligned} D_B &\cong 1.62 \pm 0.02 \text{ in two dimensions,} \\ D_B &\cong 1.74 \pm 0.04 \text{ in three dimensions.} \end{aligned}$$

Notice that it is much less dense than the percolation cluster. In particular, the probability of a site belonging to the *backbone* is given by a relationship of the form

$$P_B \propto (p - p_c)^{\beta_B}, \quad (3.1-28)$$

with  $\beta_B \cong 0.53$ . On the other hand, its correlation length is equal to that of the percolation cluster itself. Lastly, its *ramification* is finite.

### 3.1.2 Evaporated films

Thin evaporated metallic films give rise to disordered structures of the percolating variety. Electron transmission micrographs have been taken of evaporated gold films with an amorphous  $\text{Si}_3\text{N}_4$  substratum (Voss et al., 1982).

Fig. 3.1.9, (b) shows three connected clusters from micrograph (a) in which the concentration is  $p = 0.64$ : the set in black is the largest cluster. The authors studied layers of varying concentrations and determined the percolation threshold (which is not universal) and various exponents including  $\tau$ , which gives the distribution of clusters of a given surface area. The measured value of  $\tau$  is in agreement with the theoretical value in  $d = 2$ , namely  $\tau \cong 2.05$ .

Similarly thin layers of lead deposited on amorphous germanium have been analyzed by Kapitulnik and Deutscher (1982). The analysis of the digita-

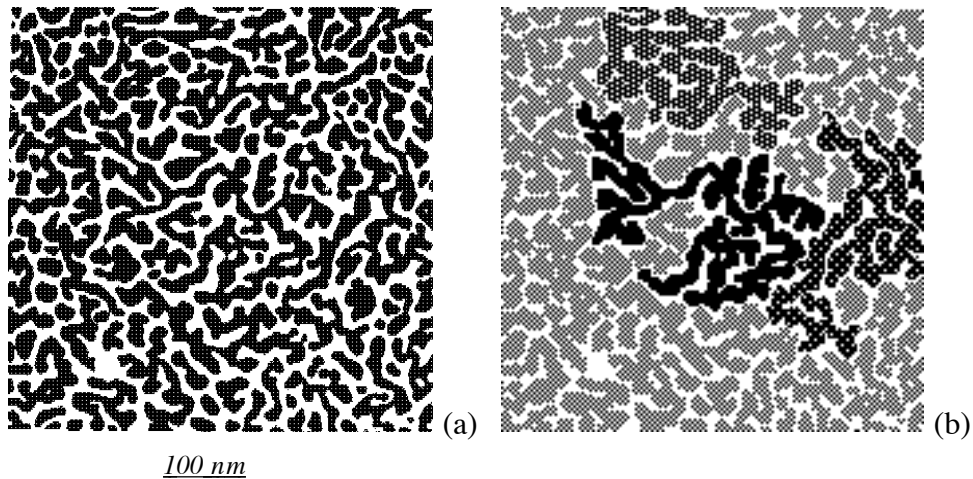


Fig. 3.1.9. (a) Digitalized image of an evaporated gold film on an amorphous substratum of  $\text{Si}_3\text{N}_4$ . (b) From this image three clusters have been extracted. The concentration of gold coating is  $p = 0.64$ . The threshold,  $p_c$ , was found to be approximately 0.74 (Voss et al., 1982).

lized images is shown in Figs. 3.1.10 (a) and (b).

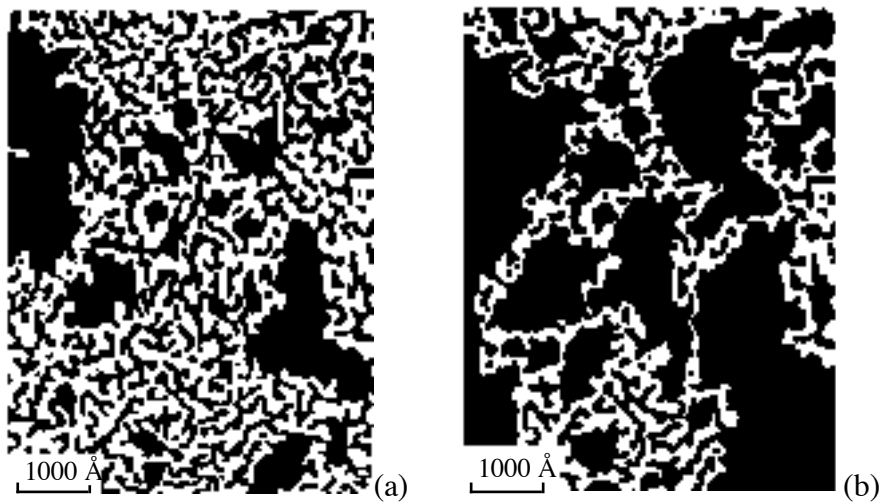


Fig. 3.1.10. Deposit of Pb on amorphous Ge. (a) Part of the infinite cluster, (b) the backbone (Kapitulnik and Deutscher, 1982).

The fractal dimension found here is  $D = 1.90 \pm 0.02$  (in the percolation model,  $D = 1.89\dots$ ). The correlation function (i.e., the density) has also been found and this suggests a value of the exponent ( $D - d$ ) in agreement with the value of  $D$ . Lastly, the backbone, the part of the infinite cluster able to conduct a continuous current, has fractal dimension  $D_B \cong 1.65 \pm 0.05$ , which also agrees with the percolation model.

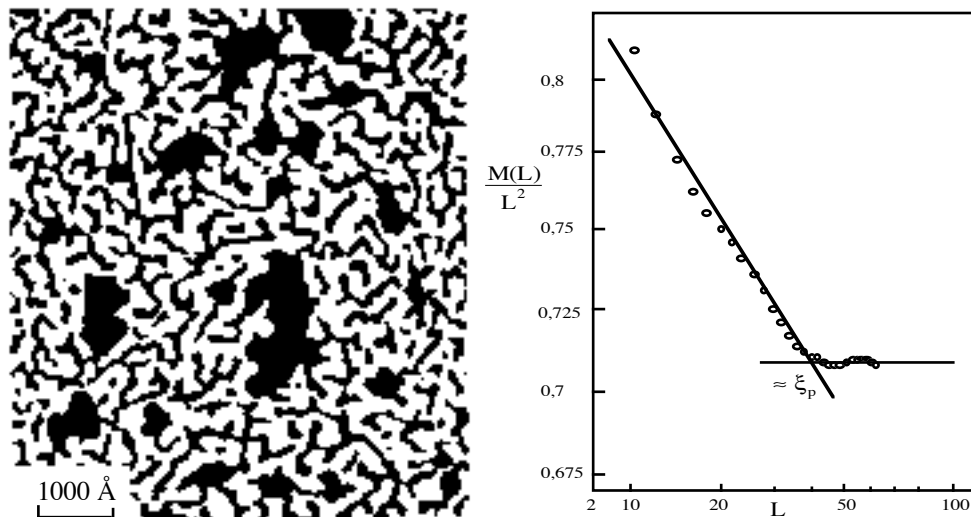


Fig. 3.1.11. Part of the infinite cluster at a covering concentration greater than the threshold. On the right is shown a log-log graph of density against size. The structure is fractal at scales up to  $\xi_p \cong 40$  Å and then becomes homogeneous (constant density) (Deutscher et al., 1983)

At concentrations greater than the percolation threshold (Fig. 3.1.11), the structure is fractal at scales up to a critical distance  $\xi_p$ , while at scales greater than this distance the dimension is found to be 2. As in the previous example, the authors have calculated the distribution of clusters of surface area  $s$ , and they have found that  $n_s \propto s^{-2.1 \pm 0.2}$ .

### 3.2 Porous media

A porous medium is a randomly multiconnected medium whose channels are randomly obstructed. The quantity that measures how “holed” the medium is due to the presence of these channels is called the *porosity*,  $C$ , of the medium. Another important physical quantity, analogous to the conductivity,  $\sigma$ , of a network of resistors, is the *Darcy permeability*: It decreases continuously as the porosity decreases, until a *critical porosity*,  $C_{cr}$ , is reached when it vanishes. Below this level of porosity the medium is no longer permeable (the residual porosity is said to be closed), while above it there is a path crossing the medium, i.e., an infinite “cluster.”

A fractured granitic rock is an example of a poorly connected porous medium. The plane fissures can be roughly modeled by disks of random direction, position, and size.

If the distribution of channels or fissures is random and the large scale correlations in the channel structure are negligible, then transport in a porous medium resembles current flow in a random resistor network; in other words, it is related to the problem of percolation. Therefore, we might expect permeability to be characterized by a *universal behavior* that depends solely on the Euclidean dimension of the space and on the relative distance from the threshold, but which does not depend on all the microscopic details, order and nature of the connections, etc. The variation in the *permeability* close to the threshold ought to be expressible in the form

$$\begin{aligned} K &= K_0 (C - C_{cr})^\mu, & C > C_{cr}, \\ K &= 0, & C \leq C_{cr}, \end{aligned} \quad (3.2-1)$$

where only the factor  $K_0$  depends on these microscopic details. Of course in reality the situation is much more complex (especially due to problems of interfacial physicochemistry in the divided material). This approach via percolation theory must thus be considered as merely a powerful framework for understanding the statistics of these systems.

Furthermore, modeling a porous medium by bond or site percolation is imprecise due to the fact that the network is disordered as much from the point of view of the shape of the pores as of their interconnections (Fig. 3.2.1). However, it is known (by universality) that this does not affect the behavior (i.e., the power laws), but only the prefactors and critical values of the parameters ( $C_{cr}$  for example) which depend on the microscopic texture of the

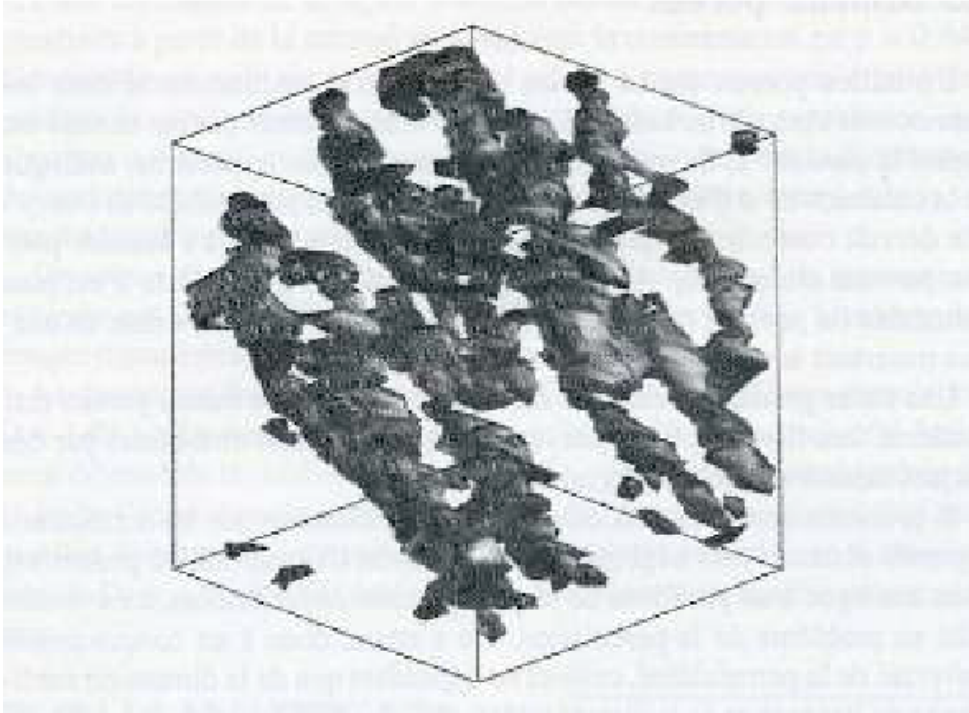


Fig. 3.2.1. An example of Fontainebleau sandstone from samples provided by C. Jacquin. The pores are light. (Image kindly provided by P.M. Adler.)

material.

Two *empirical relations* have been relatively well established for a large variety of lattices (see Table II): the product  $z p_{Bc}$  is within less than 0.06 of 2, when  $d = 2$ , and of 1.5, when  $d = 3$ , and the product  $f p_{Sc}$  is within 0.015 of 0.45, when  $d = 2$ , and of 0.15, when  $d = 3$ , where  $f$  is the filling factor of the lattice obtained by inscribing spheres of radius equal to half of the distance to the closest neighbor ( $f$  is the percentage of the total volume occupied by these spheres).

First of all, let us review some of the more interesting physical phenomena connected with porous media. These are primarily cases of transport phenomena. The question of how a fluid flows across a medium concerns monophasic flow, which is explained in Sec. 3.2.1. Another very important aspect, as much from the point of view of the fundamental physics involved as from, say, that of the extraction of petroleum from certain rocks, is the question of how a fluid injected into a medium displaces one that has already impregnated its pores; this is described in Sec. 3.2.2.

### 3.2.1 Monophasic flow in poorly connected media

Two main types of porosity can be distinguished. In the first type the holes are practically interconnected: this is so in the case of soils (pores not consolidated) and in the case of sandstones (pores consolidated) (Fig. 3.2.1).

The second type corresponds to nonporous, but fissured, rocks: in this case there are many connected regions of fissures (“finite clusters”) with, in media that are permeable, one or more clusters extending from one end of the rock to the other (which may thus be considered as precursors of the infinite cluster of a percolating network).

The first type has already been extensively studied by physicists working on porous media. For the most part *mean field* or *effective medium* methods have been employed to homogenize the disordered medium of the pores. Various methods are possible (e.g., the self-consistent method, described above [Eq. (3.1-7)] in the calculation of  $P_\infty(p)$ , or a simple homogenization process), but none of them is capable of explaining the behavior of the media in the neighborhood of the percolation threshold.

Similarly, no classical method is able to describe the critical behavior of fissured rocks at the moment they become permeable. Even the self-consistent methods, which account for the percolation threshold, do not give the correct values of the critical exponents (these models imply that the permeability varies linearly with the distance from the threshold,  $C - C_{cr}$ , and that  $\mu = 1$ ). It will therefore be necessary to use methods better suited to critical phenomena.

If a pressure difference  $\Delta P$  is applied between two opposite faces of a porous medium with cross-sectional area  $A$  and length  $L$ , a flux,  $Q$ , of fluid is established, given by *Darcy's law*,

$$Q = \frac{K A}{\mu} \frac{\Delta P}{L}, \quad (3.2-2)$$

where  $\mu$  is the viscosity of the fluid. It is of the same form as Ohm's law.

The physics of monophasic flow is related to the medium's permeability, that is, to the geometry of the connected clusters (for more details consult, e.g., P. M. Adler in Avnir, 1989). If the pores are interconnected, a mean field calculation proves sufficient; however, in fissured but nonporous rocks close to critical porosity, a percolative approach is necessary. In what follows, attention will be focused on systems in which two fluids are present in a porous medium. This situation gives rise to a rich variety of phenomena in which fractal structures are often present.

### 3.2.2 Displacement of one fluid by another in a porous medium

When a fluid is displaced by the injection of a second fluid, the observed phenomena are naturally highly dependent on the relative properties of the two fluids.

First, they may be *miscible* (alcohol and water, etc.) or *immiscibles* (air and oil, mercury and water, etc.). Moreover, when immiscible fluids are found in porous media, one of the fluids is said to be *wetting* (i.e., it has a tendency to advance along the walls) and the other *nonwetting*: for example, in the case of water and mercury, water is the wetting fluid. The “wettability” is characterized by the angle,  $\theta$ , which the interface makes with the wall (Fig. 3.2.2). A fluid is perfectly wetting when  $\theta = 0$ .

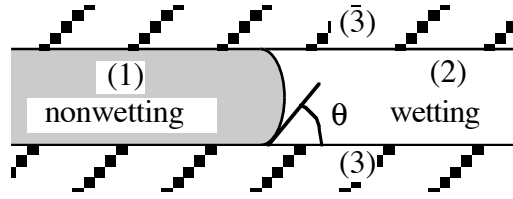


Fig. 3.2.2. Interface between two fluids (1 and 2) at equilibrium in a channel of the porous medium (3). The angle  $\theta$  depends on the three surface tension couples  $\gamma_{12}$ ,  $\gamma_{23}$ , and  $\gamma_{31}$ . The curvature of the interface induces a pressure difference between the two fluids.

An important characteristic of the interface between two fluids is the existence of an interfacial tension,  $\gamma$ , which induces a pressure difference,  $P_{cap}$ , on either side of the interface of these fluids meeting in a channel of radius  $r$ .

This pressure difference, called capillary pressure, may be expressed as

$$P_{cap} = 2 \gamma \cos \theta / r \quad (3.2-3)$$

Displacements of one fluid by another are governed by *Poiseuille's law* (similar in form to *Darcy's law*): the volume flux,  $Q_s$ , in a channel of length  $a$  and radius  $r$  joining two pores  $i$  and  $j$ , in which the pressures are  $P_i$  and  $P_j$  respectively, (Fig. 3.2.3) is given by

$$Q_s = \frac{\pi r^4}{8 a \mu} (P_i - P_j - P_{cap}) \quad (3.2-4)$$

In this expression  $\mu$  is the effective viscosity obtained by weighting the viscosities  $\mu_1$  and  $\mu_2$ .

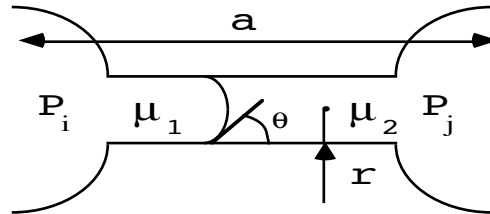


Fig. 3.2.3. Schematic representation of the channel joining two pores  $i$  and  $j$  of a porous medium in an injection experiment.

If  $(P_i - P_j) > P_{cap}$ , the nonwetting fluid displaces the wetting fluid ;  
 if  $(P_i - P_j) < P_{cap}$ , the opposite occurs.

Moreover, when the rate of injection is very slow the capillary forces (surface tension, etc.) dominate, whereas when it is very rapid the viscosity forces dominate.

Essentially there are three factors at play in quasistatic injection experiments (where capillary forces dominate):

- (i) The external conditions imposed, such as the pressure or constant rate

of flow;

(ii) the incompressibility of the fluid to be displaced (trapping problems); and

(iii) the direction of the displacement: *drainage* occurs when the wetting fluid is displaced by the nonwetting fluid (Fig. 3.2.4); *imbibition* is the reverse process.

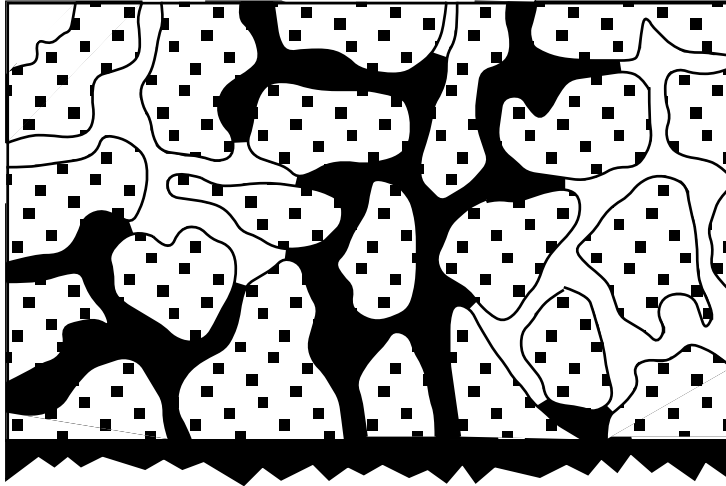


Fig. 3.2.4. Example of percolation in porous media: porosimetry by injection of mercury.

We shall not be discussing imbibition in this book since its description is slightly complicated by the presence of hysteresis phenomena (see Fig. 3.2.8), nor does it shed much further light on the aspects of greatest interest to us, the appearance of fractal structures. We mention simply that, loosely speaking, imbibition may be modeled by site percolation, in contrast to drainage which may be modeled by bond percolation, and that the imbibition process is dominated by effects arising from the presence of a thin film (wetting liquid) which acts as a precursor to the principle front (compare, for instance, Figs. 3.2.7 and 3.2.8 below).

### 3.2.3 Quasistatic drainage

The injection of mercury under vacuum at constant pressure is a very common method of measuring the porosity and pore sizes of a rock. A sample of rock with its interstitial water removed is placed in a vacuum and plunged into a bath of mercury: The quantity of mercury injected is measured in relation to the injection pressure.

The mercury does not wet the rock, so that it can only cross a passage between pores if the radius  $r$  is sufficiently large for the capillary pressure,  $P_{cap}$ , to equal the injection pressure,  $P_{inj}$  (Fig. 3.2.5).

At a given pressure,  $P$ , the mercury only penetrates channels whose dia-

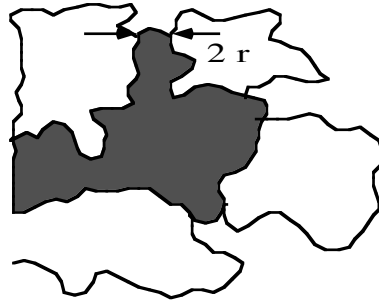


Fig. 3.2.5 Injection of a nonwetting fluid, blocked by the presence of narrow passages of maximum dimension  $2r$ , requiring a pressure increase in the injected fluid,  $P_{cap}$  inversely proportional to  $r$ .

meter is greater than  $(2\gamma \cos \theta)/P$  (where  $\gamma$  is the surface tension of the mercury and  $\theta$  the angle of junction of the meniscus;  $\theta \cong 40^\circ$  for Hg); the injection of the fluid is thus, as we shall see, analogous to the search for a connected percolation cluster at the face where the fluid enters.

The corresponding percolation problem is the following: bonds for which  $P_{cap} < P_{inj}$  will be considered closed (occupiable), the rest open (not occupiable). The set of clusters composed of “occupiable” bonds is constructed, but only those clusters in contact with the face through which the injection enters will be filled with fluid. Let us suppose that the network of channels is represented by a simple square lattice on each bond of which is shown the capillary radius (radius of the narrowest passage between two pores) needed to pass from one pore to the other (to simplify matters we consider a reduced radius  $0 < r < 1$ ) (Fig. 3.2.6). Depending on the distribution of the channels’ radii, there will be a greater or smaller proportion,  $p$ , of occupiable channels: for  $p = p_c = 1/2$  (for the square bond lattice), the percolation threshold is attained. This proportion  $p_c$  corresponds to a critical pressure  $P_c$ , which is such that for  $P = P_{inj} > P_c$  the fluid traverses all of the porous medium.

It may be observed, both experimentally and numerically, that the larger the dimensions of the rock are, the more abrupt is the transition at the threshold. Finite size effects occur since, in a section of the sample of thickness  $L$ , clusters of size greater than  $L$  allow percolation to occur and this may happen when  $P < P_c$ . Similarly, above  $P_c$ , impassable bond clusters (empty clusters) of size greater than  $L$  may occur, and these require  $P$  to be increased further beyond  $P_c$  for percolation to take place. Statistically, this translates to an apparent displacement of the threshold, already mentioned above [Eq. (3.1-17)].

### **Mercury injection at a constant rate**

The rate of injection is arranged to be sufficiently slow for the pressure of the injected mercury to be the same at each point, but such that, unlike in the previous case, this pressure can vary.

We start with the system in a given state at a particular moment. As the rate of injection is constant the curvatures of all the menisci increase. The

pressure grows until the moment when the widest passage faced by the set of these menisci is crossed, which momentarily fixes the pressure of all the menisci at the value of the capillary pressure of this passage. The fluid then invades the corresponding pore and the pressure decreases slightly; the other menisci in the neighboring passages recede. (This mechanism of pressure fluctuation is sometimes called a “Haines jump”.) In this process of quasistatic injection, the pressures reach equilibrium and so at each moment the curvatures of the menisci are equal.

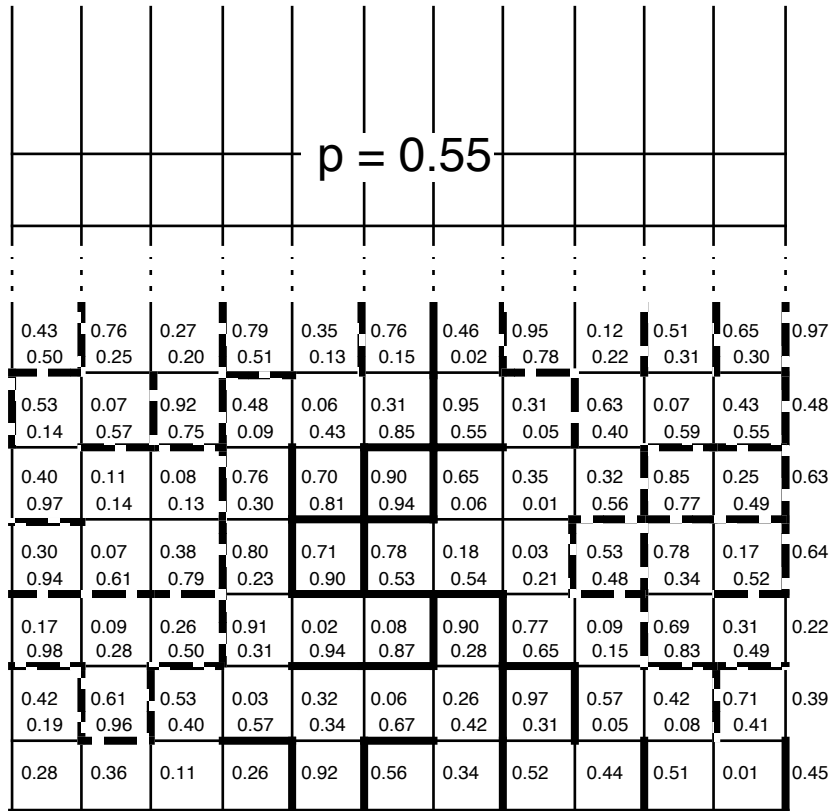


Fig. 3.2.6. The pressure is sufficiently great here that all the channels (bonds) of radius  $r > r_0 = 0.45$  are invaded by the fluid. As the distribution of  $r$  is assumed to be uniform over the interval  $[0,1]$ , a proportion  $p=0.55$  of the bonds (in gray) are potentially active. Some of the bonds (in black), in contact with the source, have already been invaded.

Since the fluid passes through the widest passage, numerical simulation (see Fig. 3.2.6) may be undertaken by the construction of a network of passages with random connections, approximating the real medium. However, the network may equally well be chosen to be a square ( $d=2$ ) or simple cubic ( $d=3$ ) lattice because here we are concerned with universal behavior. Numbers are then allotted to the passages at random in decreasing order of radii. Each time a passage is crossed, the one with the lowest allotted number (the largest

radius) is chosen next. Since the pressure is not fixed, there are no *a priori* definitively active or forbidden links. This mechanism is known as *invasion percolation*.

Remark: during a drainage process in which the displaced fluid is incompressible, the fluid may become trapped in certain regions, unlike in the situation shown in Fig. 3.2.7 where channel (2) becomes filled. This effect is negligible in three dimensions but not in two dimensions, where, if it occurs, it

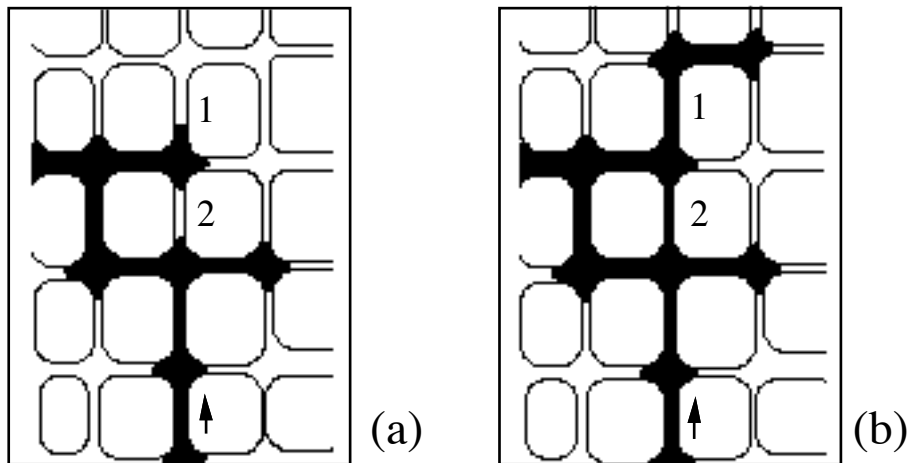


Fig. 3.2.7. Drainage: Injection through the lower face of a nonwetting fluid (in black) displacing a wetting fluid (in white) in the channels (1), and along the walls (2). In the experimental model the channels have an average cross-sectional area in the order of a  $\text{mm}^2$  and a length of 4 mm.

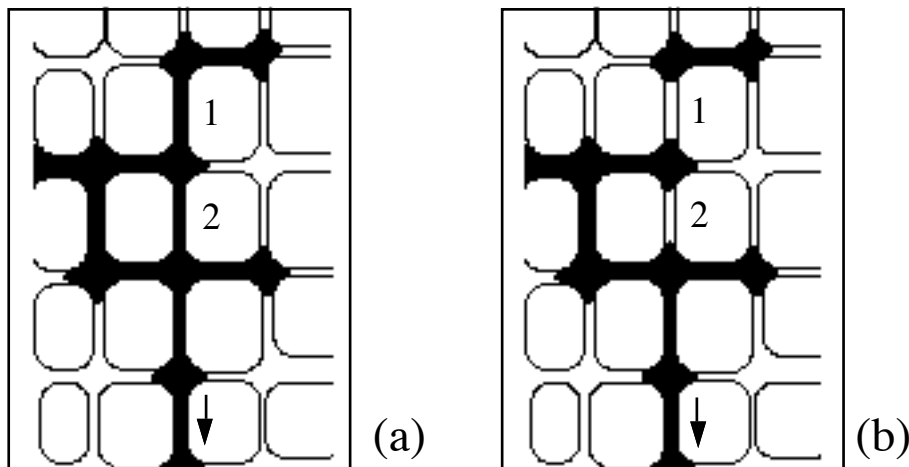
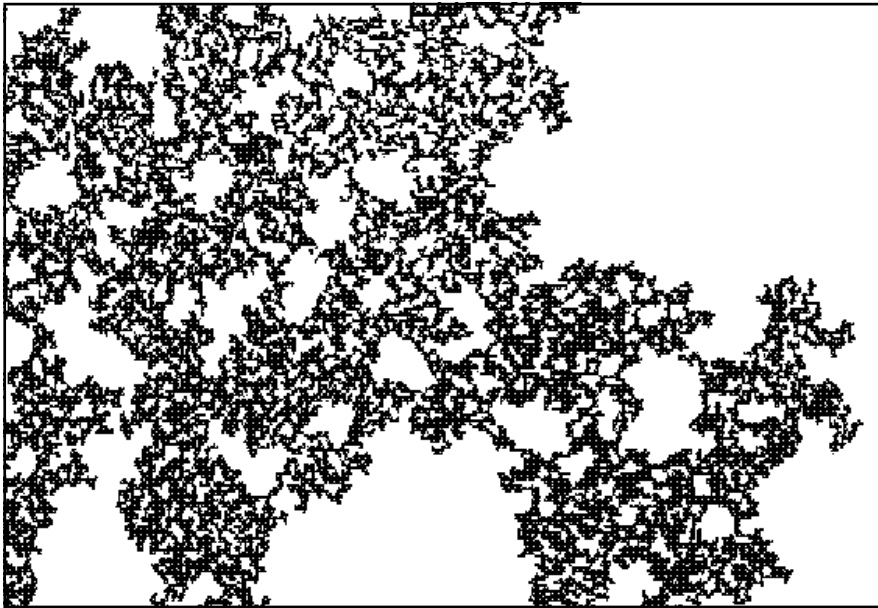
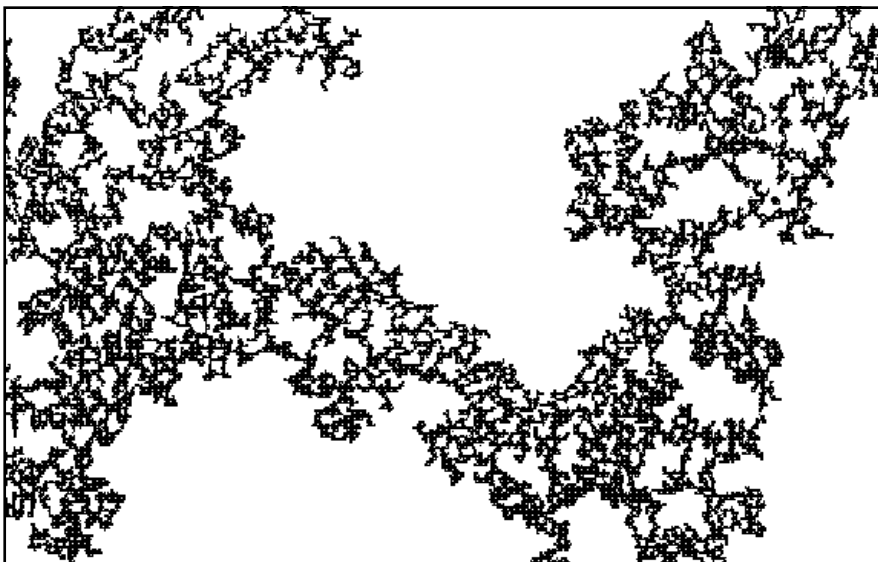


Fig. 3.2.8. Imbibition: The nonwetting fluid (in black) is displaced here by the wetting fluid (in white) injected from above. Parts of the fluid may remain trapped (1) rendering the drainage-imbibition process irreversible; whereas channel (2) is invaded by the wetting fluid. (Cf. Lenormand et al., 1983 for further details.)

dominates. Numerical simulations have shown that the dimension of the invaded cluster is close to 1.82, compared with a value of 1.89 for percolating clusters with no trapping (Figs 3.2.9 and 3.2.10).



*Fig. 3.2.9. Numerical simulation of invasion percolation following the method described earlier in Fig. 3.2.6. Its fractal dimension is equal to that of the infinite percolation cluster ( $D=91/48$  in  $d=2$ ) (after Feder, 1988).*



*Fig. 3.2.10. Numerical simulation of invasion percolation with trapping (corresponding to an incompressible fluid some of which cannot be displaced during injection). The trapped zones dominate, and the fractal dimension is reduced to  $D\cong 1.82$  (Feder, 1988).*

A precise comparison between the numerical approach and experiment has been made by R. Lenormand and his colleagues (1988). This study concerns drainage under various conditions, namely, quasistatic drainage leading to capillary fingering, and rapid drainage leading either to viscous fingering or to a stable displacement. There are two important parameters governing the behavior of these different situations: first, the *capillary number*  $C_a$  defined by

$$C_a = \frac{Q \mu_1}{A \gamma \cos \theta}, \quad (3.2-5)$$

(where fluid 1 is the injected fluid), which is the ratio between the viscous forces and the capillary forces; and second, the ratio of the viscosities of the fluids present,

$$M = \frac{\mu_1}{\mu_2}. \quad (3.2-6)$$

Lenormand et al. (1983, 1988) have studied fluid displacement in two-dimensional models made of transparent resin. The lattice of channels is positioned horizontally to avoid gravitational effects. The channels have a rectangular cross-section (1 mm x y mm), where the smaller dimension (y) varies randomly according to a scheme similar to Figs. 3.2.7 and 3.2.8, and they form a square lattice whose mesh size is 4 mm. On the basis of their experimental observations, associated with the numerical simulations, the

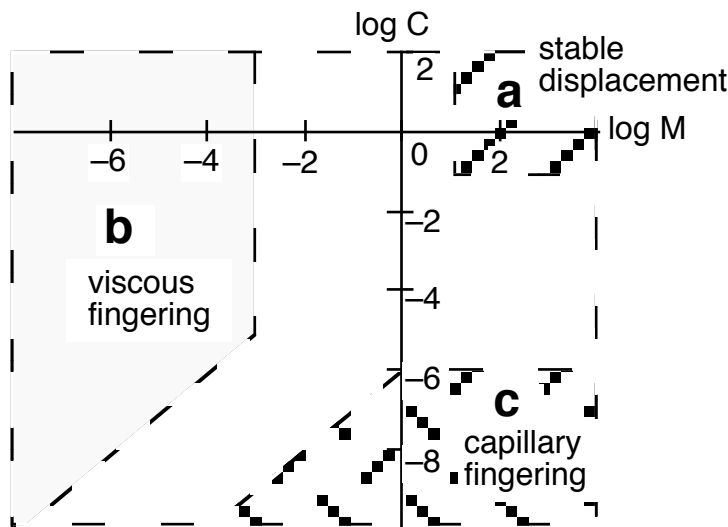


Fig. 3.2.11. Phase diagram of the drainage of a nonwetting fluid in a porous medium. There are three distinct behaviors corresponding to three distinct universality classes. Capillary fingering, described in this section, is linked to the percolation model. Viscous fingering is modeled by what is called diffusion-limited aggregation (DLA). Lastly, stable displacement, which does not generate a fractal structure, is modeled by anti-DLA (after Lenormand et al., 1988).

authors have proposed a phase diagram which enables the various dynamical situations to be classified as a function of the two parameters  $C_a$  and  $M$ . This phase diagram is shown in Fig. 3.2.11. Capillary fingering, which will be explained later in this section, corresponds to low values of  $C_a$ , that is, to an injection slow enough to be considered as a series of equilibria. This is only possible for large values of  $M$ , when the viscous forces of the injected fluid dominate. This situation is modeled by *invasion percolation* described above.

Measurements of the fractal dimension found in drainage experiments, which were carried out by Lenormand and Zarcone in 1985, using these two-dimensional lattice models for various values of the capillary number  $C_a$  (Fig. 3.2.12), are in good agreement with the theoretical value  $D = 1.82$ , which is obtained when trapping is taken into consideration (except for the value,  $C_a = 1.5 \times 10^{-6}$ , when the method used to find  $D$  proves invalid).

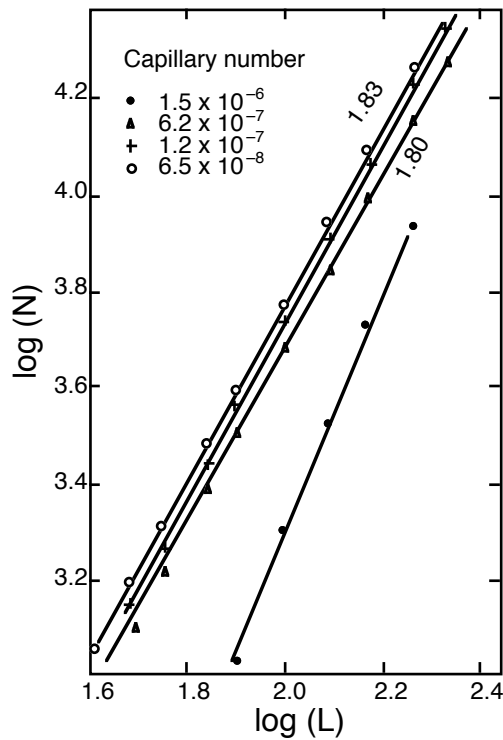


Fig. 3.2.12. Number of channels filled by air draining paraffin oil in a square lattice of size  $L \times L$ , for different values of the capillary number. The slopes 1.80 and 1.83 were obtained by the method of least squares (Lenormand and Zarcone, 1985).

The other two regimes (Fig. 3.2.11, regimes a and b) are not quasistatic; dynamic correlations are present between distant points in the fluid. The models are very different in this case and will be examined in Sec. 4.2, which concerns aggregation where the method of growth is closely analogous, as we shall see, to viscous fingering (stable displacement also introduces long range correlations but does not generate fractal structures).

Fig. 3.2.13 shows two plates obtained by the invasion of mercury into a two-dimensional porous model. The logarithm of the ratio  $M$  of the viscosities of mercury and of air is 1.9. The injection rate is controlled so that  $\log C_a = -5.9$  in (a), and  $\log C_a = -8.1$  in (b). We are well within the capillary fingering region. These structures are comparable to those of invasion percolation (Fig. 3.2.10).

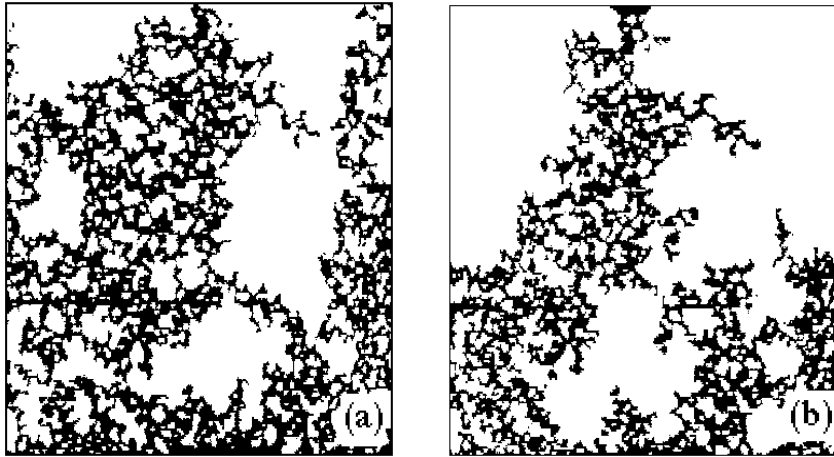


Fig. 3.2.13. Mercury (in black) displacing air ( $\log M = 1.9$ ). The injection is slower in (b),  $\log C_a = -8.1$ , than in (a),  $\log C_a = -5.9$ , but the difference is not decisive. Systems (a) and (b) are both in the capillary fingering region (Lenormand et al., 1988).

### 3.3 Diffusion fronts and invasion fronts

When an electrical contact is created between two metals, we usually think of their interface as a regular surface. In fact it is nothing of the sort. An interface created by diffusion is in general extremely irregular. Its surface area grows indefinitely with the duration of the diffusion, as does its width; its structure eventually becomes fractal within a certain spatial domain.

To model diffusion fronts we shall take the simplest system, composed of a lattice of sites and diffusing particles which jump from site to site (Fig. 3.3.1). The latter diffuse either with a probability which is the same for all particles (noninteracting), or with one which depends on the neighboring particles (attractive or repulsive interaction). In all these cases (even the noninteracting one) the particles are taken as being approximately hard spheres such that no two particles may be present at the same site. We say that they have a “hard core.”

#### 3.3.1 Diffusion fronts of noninteracting particles

An example of this is when rare gases are adsorbed along the well cleaned face of a crystal: The crystalline surface creates a periodic potential

with preferred sites where the rare gas atoms localize. It can be shown that in this lattice gas model, despite the correlation between particles due to their “hard cores,” the particle density time-evolution equation is a simple diffusion equation with, in the simplest cases, a diffusion coefficient  $\mathcal{D} = z \alpha a^2$ , where  $a$  is the lattice spacing,  $z$  the number of neighboring sites, and  $\alpha$  the probability of a jump per unit time.

Clearly the presence of hard cores must influence the evolution of the particles in a system which, due to the impossibility of a site being doubly occupied, cannot be the same as that of a system of independent particles. This effect appears in pair or higher order correlations, but has no influence on the properties we are considering here, which only involve the density-density correlation. This density remains uncorrelated.

The distribution of diffused particles at a given time can be determined in the following manner. First, a solution is found for the diffusion equation with the boundary conditions imposed by the problem. Then the particles are distributed over the lattice with a probability for each site equal to the calculated concentration (no correlation hypothesis). This then constitutes a realization of the actual diffusion process. In a region of fixed concentration the randomly distributed particles can then be grouped in clusters (Fig. 3.3.1) whose statistical properties are determined by percolation theory (Sec. 3.1.1). In the present case, the value of this concentration  $p$  at a given moment varies with position.

This model is known as a *gradient percolation* model: all the ingredients for percolation are present (e.g., uncorrelated site occupation), but the concen-

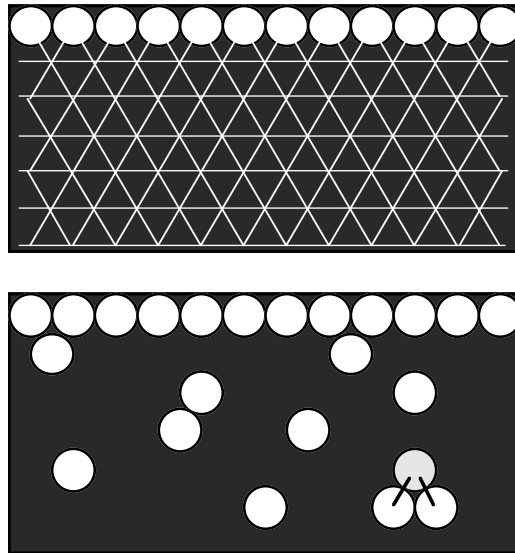


Fig. 3.3.1. Diffusion of particles over a triangular lattice. The upper figure represents the initial state: the first comb is occupied and remains so throughout the evolution. In the lower figure, some particles have diffused (the lattice has been suppressed). A cluster of three neighboring particles is shown.

tration of the sample is not uniform. A *physical property which specifies the connectivity between particles* (such as an electrical contact, or electrons jumping between atoms whose external orbits overlap, or a coupling between the nuclear spins of diffusing atoms) enables us to define connected clusters.

Taking electrical conduction as an example of such a physical property, suppose that metallic particles are made to diffuse (in direction  $x$ ) in an insulating medium (see Fig. 3.3.2). Suppose that we fix the potential  $V_0$  of the face where the diffusing metal is introduced (source). Then the set of particles in electrical contact with this source will also be at the same potential. The external surface of the collection of particles at potential  $V_0$  is known as the *diffusion front*. Beyond this, the concentration level is too low and only clusters of particles connected to one another but not to the source are found.

On condition that the concentration does not vary too much from one extremity of the cluster to the other, these finite clusters may be assumed to be distributed like those occurring in ordinary percolation in each region of concentration  $p$  of the distribution.

Similarly, the part which is connected to the source is comparable to the “infinite cluster” of ordinary percolation or, more precisely, to a juxtaposition of “infinite” clusters, corresponding to each local concentration.

### ***The two-dimensional case $d = 2$***

#### *(i) Percolation threshold*

In the two dimensional case, we find that the diffusion front remains localized in a region of concentration very close to  $p_c$ , the percolation threshold associated with the lattice and connectivity under consideration.

We can understand intuitively why this should be so since the diffusion front constitutes a path running from one extremity of the sample to the other, and were the concentration to be reduced, this path would no longer exist. The threshold  $p_c$  is situated almost exactly at the center of mass  $x_f$  of the density distribution of the frontier. It has been shown that, in cases for which no exact result is known, by constructing the diffusion front,  $p_c$  in  $d = 2$  can be determined with greater precision than any other known numerical method (see, e.g., the calculation of Ziff and Sapoval, 1986).

#### *(ii) Front width*

When a contact or an interface is created, it is important to know how its width varies as a function of the various parameters of the problem. The parameters chosen here might be the time,  $t$ , the diffusion length,  $l_D = \sqrt{(2D t)}$ , or perhaps the concentration gradient in the region of the front,  $\nabla p$ , (which varies as the reciprocal of  $l_D$ ).

As the front is in a critical region ( $p \cong p_c$ ), we should expect it to behave according to a power law in the concentration gradient. Indeed, it may be shown that the front width  $\sigma_{ft}$  varies proportionally to a power of  $\nabla p = dp/dx$  :

$$\sigma_{ft} \propto |\nabla p|^{-\alpha_\sigma} \tag{3.3-1}$$

Here,  $\alpha_\sigma = \nu/1+\nu$ , where  $\nu$  is the critical exponent of the correlation length of percolation;  $\nu = 4/3$  when  $d = 2$  (Sapoval et al., 1985).

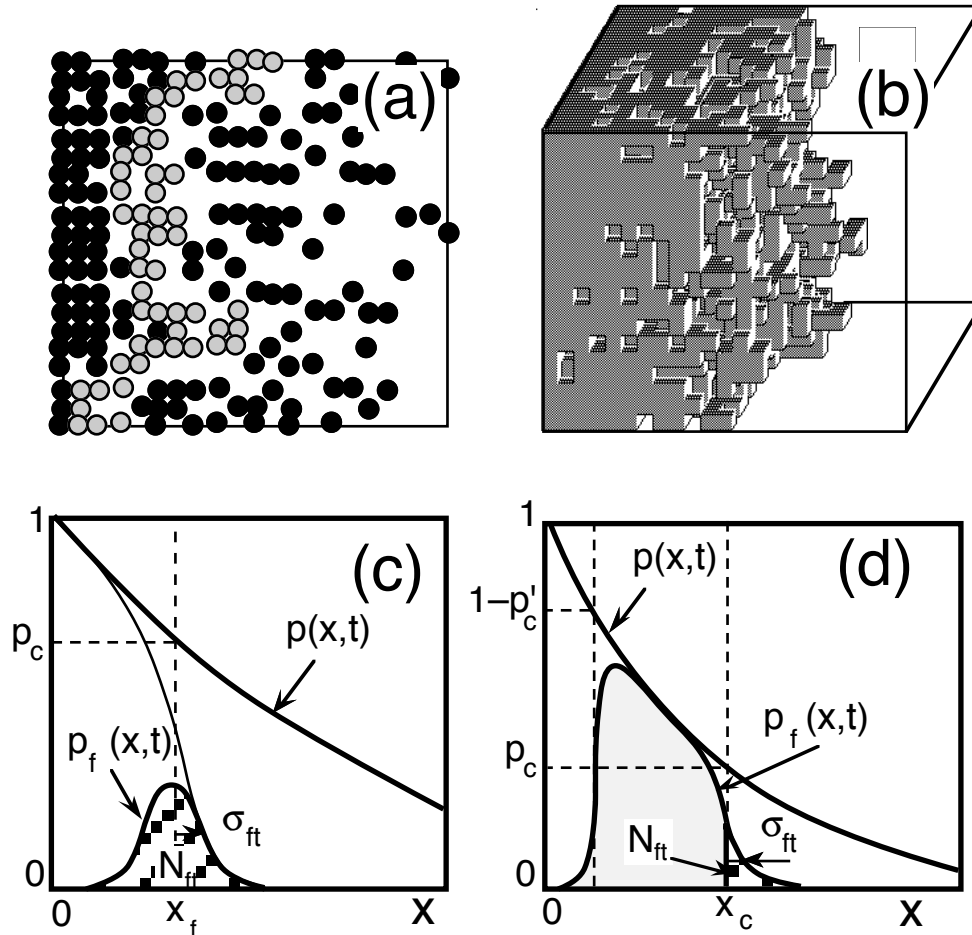


Fig. 3.3.2. Diffusion in lattices of dimension  $d=2$  [(a) and (c)] and  $d=3$  [(b) and (d)]. In figures (c) and (d),  $p(x,t)$  corresponds to the concentration profile obtained under the condition  $p(x=0) \equiv 1$  for all values of  $t$ . The shaded and hatched areas represent the diffusion front, the hatched part, of width  $\sigma_{ft}$ , being the critical region (where fluctuations are important). It is located at  $p_c$ .

To prove relation (3.3-1) we suppose that the mean cluster radius  $\xi$  at a distance  $\sigma_{ft}$  from the barycentre  $x_f$  of the frontier<sup>6</sup> (see Fig. 3.3.2) is proportional to  $\sigma_{ft}$ . Close to  $x_f$  the clusters would be too large as their mean diameter  $\xi$  diverges at  $p_c$  and so then they are nearly always connected to the front,

<sup>6</sup> Or from  $x_c$ , the abscissa of the threshold  $p_c$ , since  $x_f$  tends sufficiently rapidly to  $x_c$ :  $p(x_f) \rightarrow p_c$ .

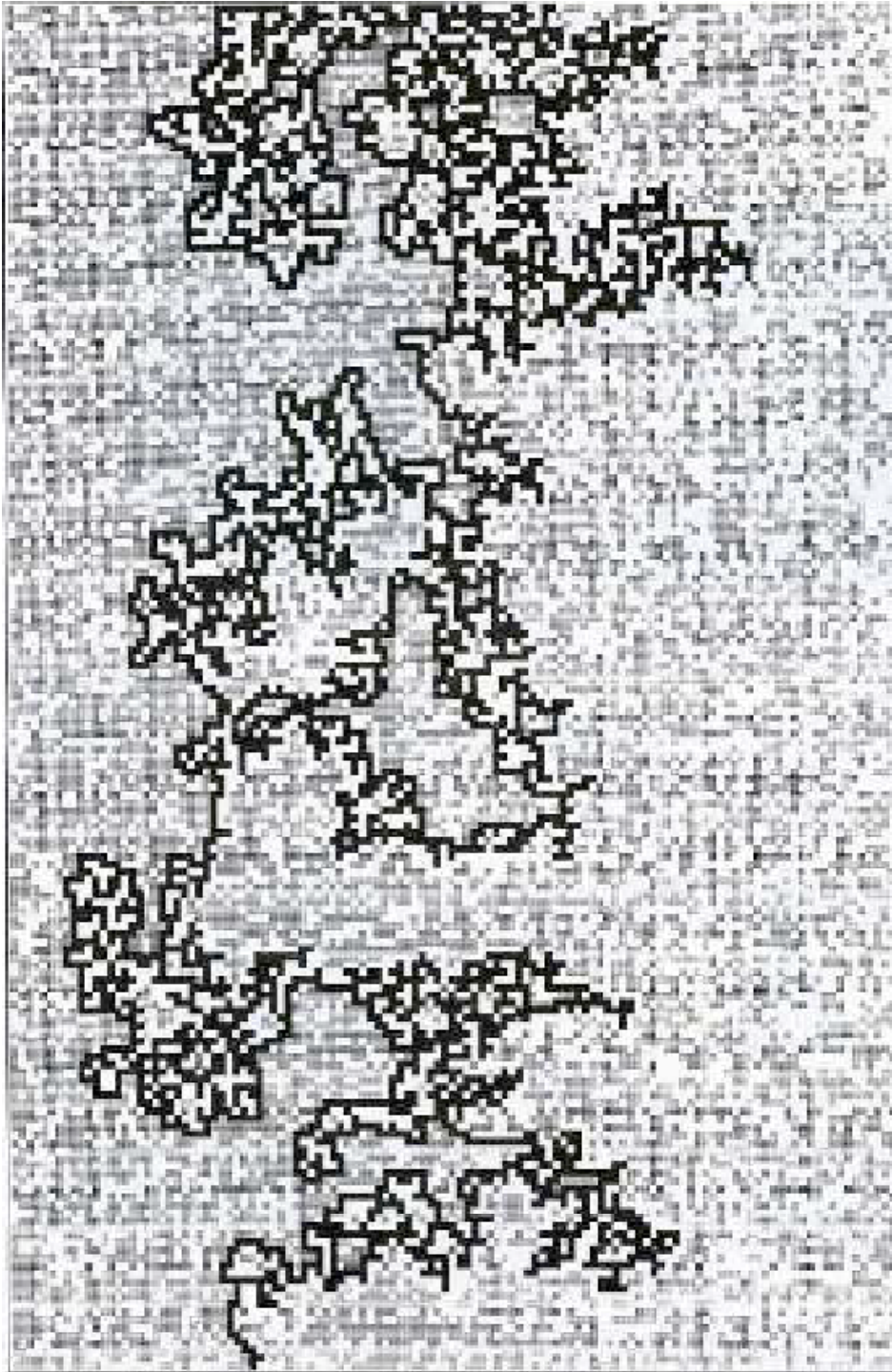


Fig. 3.3.3. Diffusion of noninteracting particles. The diffusion has taken place with the initial and boundary conditions of Fig. 3.3.2 (a), the particles being indicated by small squares. Only the region with concentration  $0.4 \leq p \leq 0.6$  has been shown. The chosen connection is between nearest neighboring sites: this enables us to determine the clusters, the infinite cluster being the one connected to the source. The diffusion front, that is, the exterior boundary of this cluster is represented in black. Its width is  $\sigma_{ft}$ , its length  $N_{ft}$  and its fractal dimension  $D_f = 7/4$ .

while far from  $x_f$  they become too small to be able to link up and remain finite clusters. Thus the region where some of the clusters are connected and some are not is defined by

$$\sigma_{ft} \equiv \xi[p(x_f + \sigma_{ft})] .$$

Using Eq. (3.1-13) and developing the above relation in the neighborhood of  $x_f$  leads to Eq. (3.3-1).

(iii) *Fractal dimension*

In a domain restricted to the width of the front, the fractal dimension is found to be

$$D_f = \frac{1+v}{v} = \frac{7}{4} \text{ in } d = 2. \quad (3.3-2)$$

The value 7/4 has been confirmed both by numerical simulations and by the use of growth models or theoretical approaches involving self-avoiding walks.

(iv) *The front length*

The front length,  $N_{ft}$  (number of particles at the interface), also varies as a power of  $\nabla p$ :

$$N_{ft} \propto |\nabla p|^{-\alpha_N} \quad (3.3-3)$$

$$\text{with } \alpha_N = \frac{v}{1+v} (D_f - d + 1) .$$

The proof of this result uses points (ii) and (iii) and the mass–radius relation. Consider the number of points of the front lying in a ball of radius  $r$ ,

– If  $r < \sigma_{ft}$  the front is fractal:

$$N_{ft}(r) \propto r^D .$$

– If  $r > \sigma_{ft}$  then we no longer see any fractal features, the front appears like a regular Euclidean surface of dimension  $d-1$  (a line in the present case where  $d = 2$ ), and

$$N_{ft}(r) \propto A (r/\sigma_{ft})^{d-1} ,$$

where  $A$  is the number of particles,  $\sigma_{ft}^D$ , within a radius of the order of the front width.

It should be noted that although the front exhibits a change of dimension depending on whether it is observed at a large or at a small scale as do self-affine structures, it is not self-affine but self-similar, truncated by the effect of the gradient and comparable to a covering of dimension  $d-1$  by self-similar fractal boxes of side  $\sigma_{ft}$ .

– The number of sites in the front for a sample of size  $L$  ( $L \gg \sigma_{ft}$ ) is therefore

$$N_{ft} = A (L/\sigma_{ft})^{d-1} \approx L^{d-1} (\sigma_{ft})^{D_f - d + 1}$$

which leads to Eq. (3.3-3).

(v) *Generation of noise in  $1/f^\alpha$*

During diffusion, the front is extremely erratic and, even when the system is almost “frozen” (no observable diffusion), interface fluctuations remain important and may be a possible source of contact noise between metals or semiconductors. The behavior of this type of noise has been studied numerically in two dimensions and theoretically in two and three dimensions (Sapoval et al., 1989; Gouyet and Boughaleb, 1989). Below a cutoff frequency,  $f_c$ , the noise is white, whereas for higher frequencies the noise is in  $1/f^2$ .  $f_c$  also varies as a power of the concentration gradient:

$$f_c \propto |\nabla p|^{-1/(1+\nu)} . \quad (3.3-4)$$

In fact, diffusion fronts belong to the very broad class of self-organized criticality (Per Bak et al., 1988), that is to say that the structure of the front organizes itself into a critical structure on either side of the threshold  $p_c$ . It is known that these self-organized critical structures may generate noise in  $1/f^\alpha$  as they fluctuate in time.

***The three-dimensional case  $d = 3$***

The principle remains the same here, yet, the structure of the front is now fundamentally different. This is due to the fact that in three dimensions the presence of a percolation path no longer bars the way<sup>7</sup> of particles closer to the source (i.e., for  $p \gg p_c$ ) since this path can now be bypassed, and so particles are found on the external surface at concentrations greater than  $p_c$ . Consequently, the front is now no longer localized at  $p_c$ . It extends over a range of concentrations stretching from  $p_c$  (percolation of the lattice of occupied sites) to a concentration  $p_{\max} = 1 - p'_c$  where  $p'_c$  may be shown to be equal to the percolation threshold of the lattice of empty sites. The two lattices composed of the occupied sites and the empty sites are said to constitute a *matching pair*. For a simple cubic lattice, for example,  $p_c \cong 0.312$  and  $p'_c \cong 0.1$ , and hence the interface extends over concentrations ranging from 0.312 to 0.9.

The general definition of a matching pair is rather intricate. For the square site lattice, the lattices with first neighbor connectivity and with second nearest neighbor connectivity make up a “matching pair.” For the triangular site lattice, the lattice with nearest neighbor connectivity is self-matching (which means that  $p_c = 1/2$ ). A matching pair of lattices in the case of a simple cube lattice are those with nearest and third nearest connectivity (see Essam, 1980 for more details).

---

<sup>7</sup> Whereas in two dimensions, the particles situated on the exterior surface (or front) are all necessarily positioned on the same side of any percolating path, that is, path of touching particles joining two opposite faces of the sample.

(i) *Critical region*

In the neighborhood of  $p_c$  (0.312 for a simple cubic lattice), the front's structure is still critical. In particular, at concentrations weaker than  $p_c$  (the front's tail), its width is given by

$$\sigma_{\text{ft}} \propto |\nabla p|^{-\alpha_\sigma} \quad \text{with} \quad \alpha_\sigma = \frac{\nu}{1+\nu}, \quad \text{where} \quad \nu \cong 0.88 \quad (3.3-5)$$

and involves a number of particles given by

$$N_{\text{ft}} \propto |\nabla p|^{-\alpha_N} \quad \text{with} \quad \alpha_N = \frac{\nu}{1+\nu} (D_f - d + 1) \quad (3.3-6)$$

following the same power laws as in the two-dimensional case (the same proofs apply), but with a different value of  $\nu$  [see Fig. 3.3.2 (b)]. The critical region is fractal and has dimension:  $D_f = 2.52 \pm 0.02$  (see table III, Sec. 3.1).

(ii) *Ideal porous media*

Over a wide range of concentrations nearly all of the particles in the infinite cluster belong to the front. This explains why the same value is found for the fractal dimensions of the front and of the infinite percolation cluster:  $D = D_f \cong 2.52$ . Thus, at  $p \cong 0.75$  only 1 in  $10^4$  of the particles of the infinite cluster do not belong to the front, and this proportion decreases considerably further as  $p$  decreases (it falls to zero in the critical region). In the intermediate region the front is homogeneous with dimension  $D_f = d = 3$ . It could be said to constitute the *perfect disordered porous medium*, since all of its mass ( $M \approx L^3$ ) is in its surface; of course this is quite unusual in that it is three-dimensional, but this should come as no surprise to us, as we already know of curves, such as Peano's, which have the same dimension as a surface (Sec.1.4.1), and which may therefore be thought of as a perfect two-dimensional deterministic porous medium.

**3.3.2 The attractive interaction case**

In the presence of an interaction between the particles, the behavior may be radically different. Indeed, below a certain critical temperature  $T_c$  a phase transition may take place. When the interaction is attractive this will be a liquid-gas transition, while in the repulsive case, which we shall not examine here, it will be an order-disorder transition. The following behavior may be noted:

*At high temperatures* ( $T > T_c$ ), the structure of the front remains similar to that occurring in the noninteractive case insofar as the scaling laws concerning the width and the surface area of the front, as well as the one concerning its fractal dimension, are all preserved. Only the small scale structures change due to the correlations between particles arising from the interaction.

*At low temperatures* ( $T < T_c$ ), the stable structure of the front is no longer

fractal, because an interface, whose width is fixed solely by the temperature, is established between the liquid phase and the gaseous phase. In Fig. 3.3.4 a diffused distribution at three different temperatures is shown.  $\beta E$  is the relevant parameter, where  $\beta = 1/kT$ , and  $E$  is the interaction energy (attractive here, so negative) between first neighbors. The transition occurs at  $\beta E \cong -1.76$ .

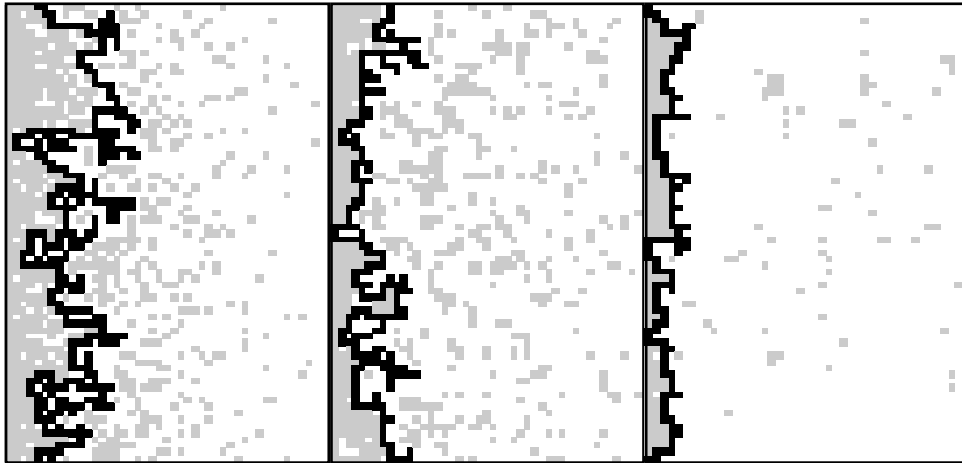
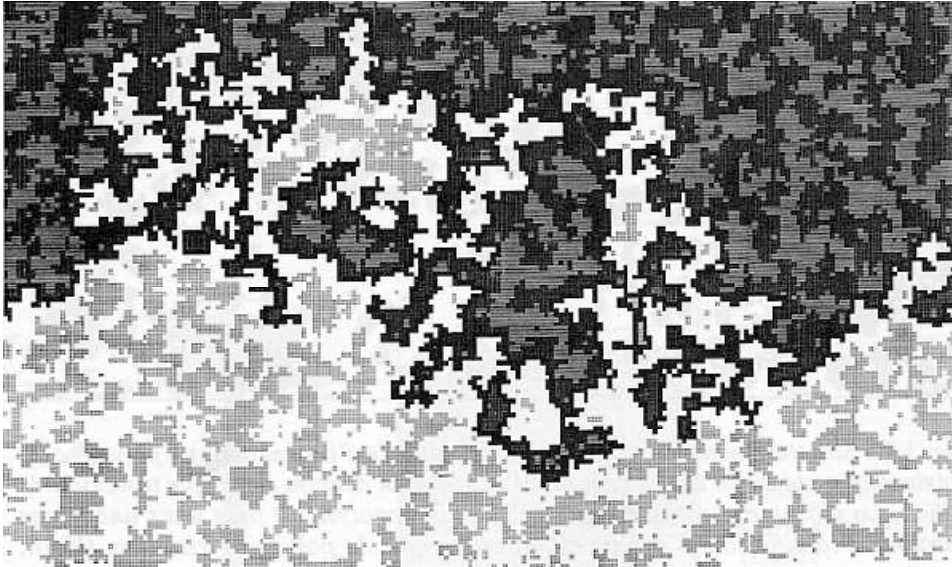


Fig. 3.3.4. Diffusion of interactive particles for three different temperatures: from left to right, respectively,  $\beta E = 0$  (no interaction),  $\beta E = -1$  (high temperature), and  $\beta E = -2$  (low temperature). The front is only fractal for  $\beta E \geq \beta E_c = -1.76\dots$  Above the critical temperature, the front has a finite width at thermodynamic equilibrium (Sapoval et al., in Avnir, 1989, p. 237).

A situation which occurs very frequently, and hence is of great interest, is when a *quench* interrupts a diffusion process. Before the quench, diffusion takes place in the high temperature region and the front is described by a *percolation gradient* model. After the quench occurs, a nucleation process develops (by spinodal decomposition). The droplets of liquid grow with time until their size approaches that of the receptacle (the phase transition has then been completed). In the regions of highest concentration these droplets form clusters, and it is then possible to verify that the model remains a percolation gradient model in which only the distance scale has been altered (renormalized): the mean droplet size, or equivalently their mean separation, replaces the intersite distance of the lattice (or the particle size for off-lattice diffusion). A structure obtained in this way by a quench starting from an equilibrium state at high temperature (the profile varies linearly from concentration 1 to concentration 0) is shown in Fig. 3.3.5 (only concentrations ranging between 0.4 and 0.6 are shown). The simulation is carried out using a Monte Carlo method and so-called Kawasaki dynamics.<sup>8</sup>

<sup>8</sup> In the lattice being considered, each particle is chosen at random and jumps to one of its neighboring sites, provided that it is empty, with a probability which depends on the interaction and a parameter  $T$ . This parameter is defined so that the particle distribution obtained when equilibrium is reached is equal to that of thermal equilibrium at temperature  $T$ .



*Fig. 3.3.5. Numerical simulation of attractive particles diffusing at high temperature followed by a quench. Droplets have been formed, some of which have linked up to form clusters (in gray). The interface is represented by the solid line. It has a fractal dimension of 1.75. The region situated between the source and the front has been superimposed on a gray background, (Kolb et al., 1988).*

### ***Examples of front structures observed experimentally***

A remarkable analysis has been carried out on a closely related model, shown in Fig. 3.3.6 (Wool, 1988). This structure is obtained by the diffusion, in the presence of an electric field, of silver chloride molecules within a polymer layer (polyimide film), and the precipitation of silver (shown in black in the image). The nucleation of the silver is very similar to that of spinodal decomposition: the clusters grow as the reduction takes place, and their concentration is proportional to the concentration of diffused silver chloride. Wool has measured a fractal dimension  $D_f = 1.74$  (against a theoretical value of 1.75) for this two-dimensional interface between the reduced silver (in black) connected to the source and the purely polymer region (in white).

The second example we shall describe here occurs when a fluid is injected into a porous medium in the presence of gravity. This example might appear somewhat remote from the case of diffusion we have just considered, but in fact this is not so. Earlier, in Sec. 3.2 on porous media, we described how drainage occurs for very slow flows. The capillary number is small and the injection may reasonably be interpreted by an invasion percolation model. Due to the presence of gravity, the fluid pressure is greater at the bottom of the region invaded by the fluid and the concentration in the pores that have been

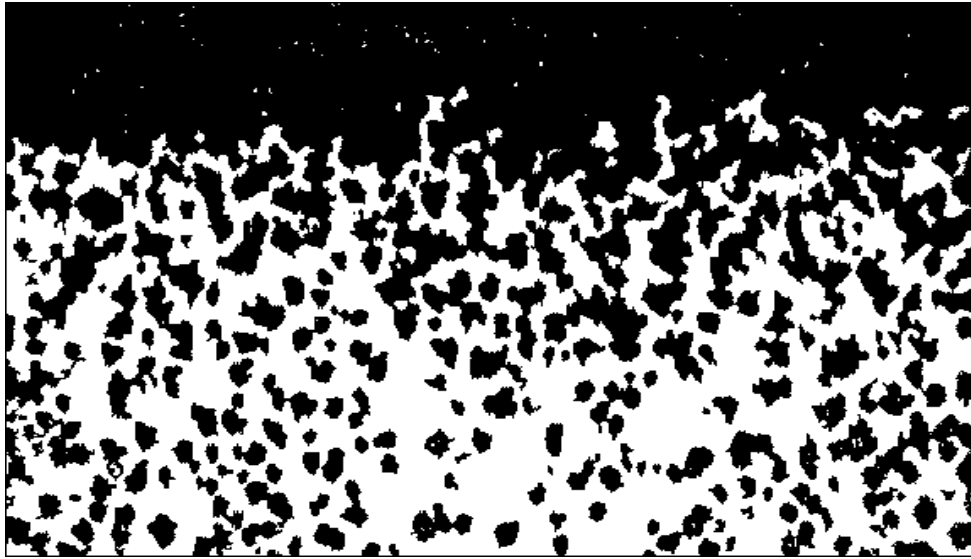


*Fig. 3.3.6. Structure obtained by diffusion of silver chloride in a polymer (polyimide) and reduction of silver under the action of an electrical field across the medium. The diffusion is three-dimensional but the analysis has been carried out in a section parallel to the diffusion. The reduced silver is in black, the polyimide in white (Wool, 1988).*

invaded is higher the lower their position. The appropriate model for this problem is called invasion percolation in a gradient. The underlying model is the same as in the case of diffusion in a gradient.

Invasion percolation in a gradient may be modeled as follows: in a lattice of size  $L^d$ , random numbers are selected between  $z/L$  and  $1+z/L$  and assigned to each site (see Fig. 3.2.6 which occurs when  $L = \infty$ ). In this way, the “resistance” to invasion grows linearly with  $z$ . Invasion begins at  $z = 0$  and continues as in ordinary invasion percolation. The process stops before the top of the lattice is reached. The invaded region corresponds to the infinite cluster of percolation in a gradient (the concentration gradient here being  $1/L$ ).

An experiment of this type has been carried out by Clément and Baudet in the following manner: a cylinder of diameter 10 cm and about 20 cm tall is filled with finely crushed glass (distance  $200 \mu\text{m}$  between pores) as uniformly as possible. Through an orifice in the bottom a liquid metal of low melting point is injected. The metal used was Wood’s metal (melting point around  $70^\circ\text{C}$ ), which is nonwetting. The injection is carried out very slowly as sketched in Fig. 3.3.7. The injection having terminated at a certain level, the system is cooled down, the metal solidifies, and the loose grains of glass are replaced with a resin. The system may then be analyzed in detail. Sections are made at various heights,  $z$ , and the correlation function between pores is determined after digitalization. As the pressure in the Wood’s metal varies with  $z$  due to gravity, so does the number of invaded pores. This can be described in fine detail using the results obtained for percolation in a gradient [the invaded region

corresponds essentially to the shaded and hatched regions of Fig. 3.3.2 (d)]. The theoretical approach compares reasonably well with the experimental results (Gouyet et al. 1989). The fractal dimension of the invasion front is found to be close to 2.4 (against a theoretical value of 2.52). In principle, this method allows the distribution of pore sizes to be determined, something which few other methods manage.<sup>9</sup>

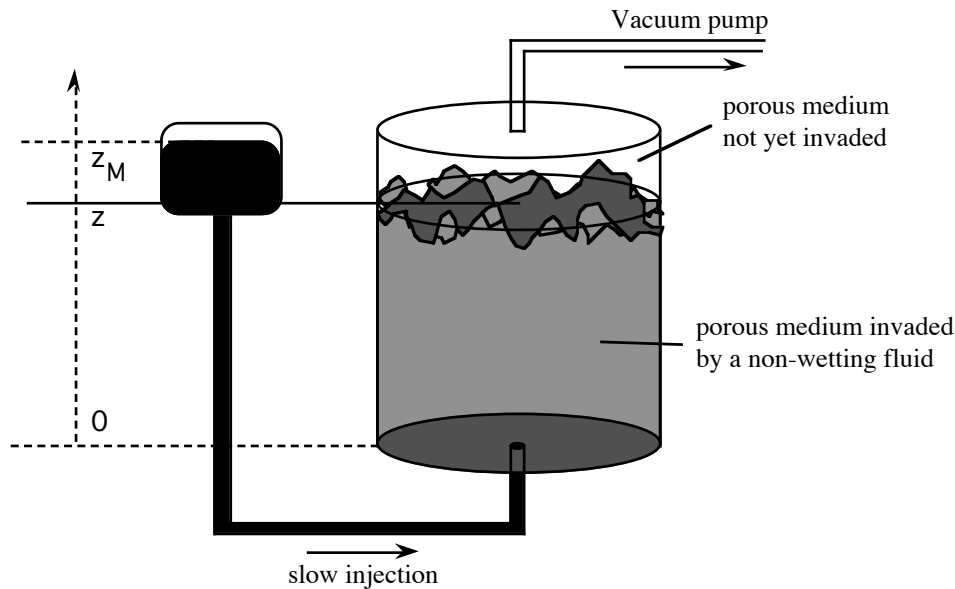


*Fig. 3.3.7. Experiment consisting of the injection of a nonwetting fluid (Wood's metal) into a porous medium (crushed glass). The Wood's metal is injected extremely slowly so as to approximate capillary fingering. The gravitational field causes the pressure to vary linearly with the height of fluid injected. The theoretical model is therefore one of invasion percolation in a concentration gradient. The theoretical results obtained earlier apply remarkably well to the experimental data and allow the various parameters of the system to be found (Clément et al., 1987).*

### **Noise generation during injection**

It has long been known that injecting a nonwetting fluid into a porous medium causes fluctuations to occur, either in the pressure, if the rate of injection remains constant, or in the rate of flow, if the pressure at the injection source is slowly increased. This phenomenon is due to the fact that whenever the fluid enters a channel of radius  $r$ , the pressure is sufficient great for it to invade all those pores which are connected to this channel by channels whose radius exceeds  $r$ . Naturally, these collections of pores form the finite clusters which appear in the corresponding percolation model (see Sec. 3.2.3). In this

<sup>9</sup> Measurements of the fractal distribution of pore sizes in resins have been made using three complementary experimental techniques by Chachaty et al. (1991). These are micropores whose radius ranges between 3 nm and 1 mm.

way, the statistical noise generated by these fluctuations is very similar to the noise in  $1/f^\alpha$  generated during a diffusion process (Sec. 3.3.1, v). Further-more, injection processes also result in self-organized critical structures. In addition to the behavior of the noise, which is white below  $f_c$  [Eq. (3.3-4)] and Brownian above it, we can also calculate  $N_{ev}(s)$  the number of events of size  $s$  (clusters of invaded pores) per unit time (Gouyet, 1990). This number obeys a power law which, at least for  $d = 1, 2$  and  $d \geq 6$ , is given by

$$\boxed{N_{ev}(s) \propto s^{-\mathcal{G}_s} \text{ with } \mathcal{G}_s = 1 + \frac{D_f - D_{red}}{D}} \quad (3.3-7)$$

Here  $D_f$  is the fractal dimension of the invasion front (equal to  $7/4$ , or often in practice, to  $4/3$ ),  $D$  is the dimension of the infinite cluster (equal to  $91/48$ ), and  $D_{red} = 1/\nu$  is the dimension of the red links (equal to  $3/4$ ), which gives  $\mathcal{G}_s \cong 1.53$  (or  $1.31$ , if  $D_f = 4/3$ ). Eq. (3.3-7) is thought to be valid in any dimensions.

### 3.4 Aggregates

Aggregation processes, with their very special characteristics, have been studied for a long time,<sup>10</sup> but it is only recently that they have started to be studied quantitatively. This is thanks to developments in two areas: fractals and the notion of scaling laws, and numerical simulations that use simple growth laws to generate aggregates. These elementary, theoretical growth processes are extremely varied and generate structures ranging from percolation to Laplacian fractals, and even the Sierpinski gasket. Consequently, for the sake of clearer exposition, we shall treat them in a separate chapter and instead dedicate this section to aggregation processes that are physically observed in nature, by presenting some experiments and the different geometries which they generate.

#### 3.4.1 Definition of aggregation

*Aggregation* is an irreversible physical process in which macroscopic structures, called *aggregates*, are built up from elementary structures (particles or micro-aggregates) interacting via mutual attraction. Here we shall concern ourselves with the geometric structure of these aggregates, and later, in Chap. 4, we shall examine the important question of their growth kinetics.

In the aggregation models studied below we shall assume that the micro-aggregates or particles have already been formed, or, in other words, that the nucleation stage is over when aggregation commences. These micro-aggregates are generally fairly compact and the distribution of their sizes is relatively uniform.

---

<sup>10</sup> Cf., in particular, the remarkable book written by the biologist d'Arcy Thompson, *On Growth and Forms*, Cambridge, 1917 (or the reedition, 1961).

We may distinguish two major processes of aggregate growth,<sup>11</sup> processes which lead to structures similar to those found in other areas of physics, such as fluid injection or dielectric discharge. These two basic models are known as cluster–cluster aggregation and particle–cluster aggregation.

In the cluster–cluster process, aggregation occurs chiefly among clusters of comparable size. In the simplest model (Jullien and Kolb, 1984), two clusters of size  $s_0$  give rise to a cluster of size  $2s_0$ : this is a totally hierarchical process as then two clusters of size  $2s_0$  produce a cluster of size  $4s_0$  and so on. In practice, systems do not remain monodisperse (i.e., only one size present at any given moment), but the nature of the polydispersity that develops is such that clusters of different sizes aggregate in a process which satisfies a global scaling law (Brown and Ball, 1985).

In the particle–cluster process, a cluster of size  $s+1$  is formed from a large cluster of size  $s$  ( $s \gg 1$ ) after the addition of a single particle. In this case, the process is highly asymmetric.

These two processes produce aggregates with very different properties. Moreover, with either process, aggregation may take place in three possible different ways: it may be limited by the reaction process, that is, a potential barrier must be overcome for sticking to take place; or limited by the diffusion process, in which case the bodies (clusters or particles) diffuse in space and stick together the moment two of them collide; and lastly, aggregation may be ballistic, the bodies move freely in space (rectilinear trajectories) before aggregating.

Table IV below displays these various combinations and the type of physical phenomena to which they apply, along with their associated fractal dimensions. Notice that reaction-limited and ballistic particle–cluster aggregation generate dense aggregates ( $D = d$ ), only their surfaces are fractal. We shall encounter this feature again when we come to look at growth models,

Table IV: A summary of different types of growth

	Particle–cluster	Cluster–cluster
Diffusion	Electrodeposition, dielectric breakdown, injection (DLA)	Colloids and aerosols (screened)
D	1.72 (d=2) 2.50 (d=3)	1.44 (d=2) 1.75 (d=3)
Ballistic	Deposition, rough surfaces, sedimentation, etc.	Aerosols in a vacuum
D	2.00 (d=2) 3.00 (d=3)	1.55 (d=2) 1.91 (d=3)
Reaction	Tumors, epidemics, forest fires, etc. (Eden)	Colloids and aerosols (lightly screened)
D	2.00 (d=2) 3.00 (d=3)	1.59 (d=2) 2.11 (d=3)

<sup>11</sup> Which should not be confused with other deterministic growth processes such as the growth of crystals.

such as the Eden model, in Chap. 4.

The classification of the examples in table should not be taken as absolute. For example, electrodeposition may only be modeled by diffusion-limited aggregation (DLA) if the ion concentration is low (the electrochemical aspect of this phenomenon is, moreover, far from clear<sup>12</sup>). Injection obeys either a percolation invasion DLA model, or an anti-DLA model, depending on the values of its parameters  $M$ , the viscosity ratio, and  $C_a$ , the capillary number (see Sec. 3.2.3). Furthermore, an aggregate may be formed under the action of several different growth models: ballistic at a certain scale, diffusion at larger ones. In this case there is a change of régime in the system (a crossover) (see, e.g., Sec. 4.2.2 on the extension of the Witten and Sanders model).

In this section we are going to describe various aggregation experiments. We shall start by looking at experiments involving aggregation of aerosols and colloids, which are best modeled by diffusion or reaction-limited cluster–cluster aggregation [a detailed study of the experimental observations of aggregation carried out by M. Matsushita, as well as a paper by P. Meakin on the numerical aspects may be found in the book edited by Avnir (1989)]. We shall then go on to mention several experiments in which diffusion-limited particle–cluster aggregation is the principle ingredient. These include the examples of layers deposited by cathodic pulverization, electrolytic deposits (under certain conditions), filtration, dielectric breakdown, and the injection of one fluid into another (again only under certain conditions). It should be mentioned here that a number of experiments described by this model, which generate similar geometries, are not strictly speaking particle–cluster processes, but are nonetheless governed by the same equations (see Sec. 4.2).

### 3.4.2 Aerosols and colloids

*Aerosols* were the first aggregates to be shown to have a fractal nature; together with colloids they represent two important varieties of aggregates.

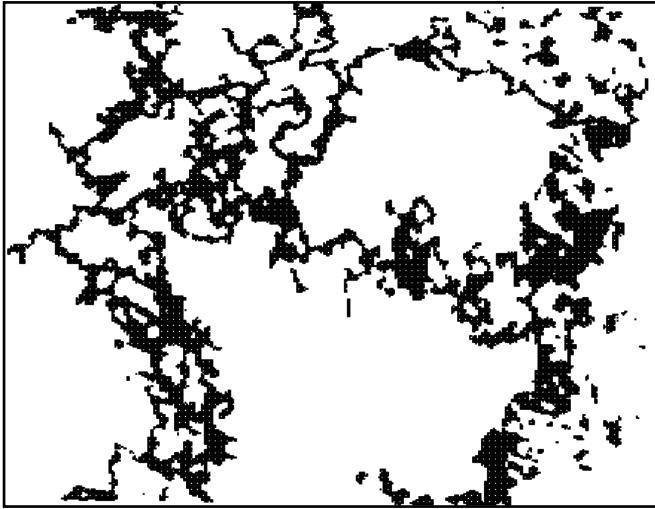
The aggregation process for aerosols is initiated by dispersing minute particles into a gaseous medium. These particles may be produced in a variety of ways: for example, smoke particles coming from the incomplete combustion of a flame; or the vaporization of a material coating a filament by rapid heating, etc.

Once dispersed throughout the gaseous medium, the particles, as long as they are electrically neutral, will behave like independent Brownian particles, except at very short distances when an attractive force (van der Waals force) causes them to group together. It should be noted however that when the gas pressure is sufficiently low (i.e., when the mean free path between collisions is large) the motion of the particles may be ballistic.

It was first observed that aggregates have fractal structures by Forrest and Witten (1979). This work was the starting point for a great many other studies which investigate the occurrence of fractal structures in aggregation and growth

---

<sup>12</sup> See, for example, the experimental work of Fleury et al. (1991) on this subject.



In 1979, Forrester and Witten were the first to study the distribution of iron particles produced by the vaporization of a heated filament in a cold, dense gas. The particles have a radius of  $35\text{\AA}$ . The fractal dimension  $D=1.51\pm 0.05$  is obtained from the mean of the masses in squares of increasing size centered randomly in the aggregate.

Fig. 3.4.1. Image of iron particle aerosols produced by a transmission electron microscope (Forrester and Witten, 1979).

phenomena. Inspired by the theory of critical phenomena, Forrester and Witten were the first to interpret aggregation in terms of scaling laws through their experience in dealing with aggregation of iron particles. They worked out the density–density correlation function  $g(r)$ , the mean centered value of the product of the densities, averaged over all pairs of points, a distance  $r$  apart, (the aggregation being assumed to be isotropic and homogeneous),

$$g(r) = \langle \rho(\vec{r}_0 + \vec{r}) \rho(\vec{r}_0) \rangle - \langle \rho(\vec{r}_0) \rangle^2, \quad r = |\vec{r}|. \quad (3.4-1)$$

This correlation function decreases according to a power law in  $r$ ,

$$g(r) \propto r^{-A} \quad \text{where } A \cong 0.3,$$

and this relation holds for various materials, suggesting a universal exponent [the measurements are made in  $d = 2$  from the digitalized image of the aggregate (Fig. 3.4.1)]. Clearly, the mass of aggregate present within a radius  $R$  in a medium of Euclidean dimension  $d$  is given by

$$M(R) \propto \int_0^R g(r) r^{d-1} dr \propto R^D. \quad (3.4-2)$$

This relates  $A$  to the fractal dimension  $D$ :  $D + A = d$ . The fractal dimension obtained by Forrester and Witten from  $g(r)$  was  $1.7 \pm 0.02$  and from the mass–radius relation  $1.51 \pm 0.05$  (the discrepancy comes from the small cluster size and the difficulty to perform good averages in the mass-radius relation).

Iron particles aggregate via a diffusion-limited cluster–cluster process (in air, iron particles move along Brownian trajectories), or, if the mean free path is not small relative to the size of the aggregates already formed, via a ballistic cluster–cluster process. The values obtained for the fractal dimension suggest

that a diffusion-limited process should be chosen here.

*Colloids* are composed of spherical microparticles (of metal, silica, etc.), a few nanometers in diameter, in suspension in a liquid. The surfaces of these particles are electrically charged and so they remain in suspension under the action of their mutual repulsion. In the absence of charged particles dissolved in the liquid, the van der Waals attraction is masked by their Coulomb repulsion (due to the electrical charges carried by these particles). In this way, the superposition of the van der Waals attraction and the Coulomb repulsion sets up a potential barrier  $\epsilon$  (Fig. 3.4.2) which is generally greater than  $kT$  and hence impassable. Such metastable solutions can survive for a very long time; indeed, there are colloids made by Faraday more than 130 years ago still in

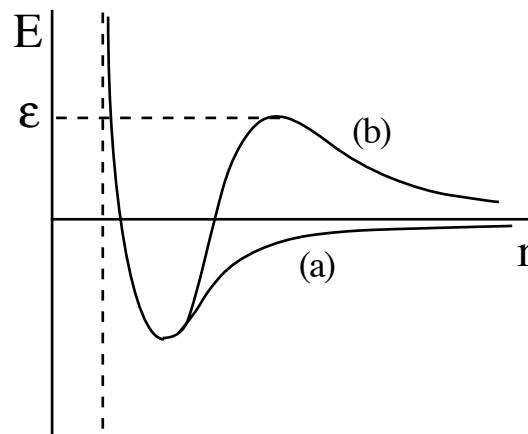


Fig. 3.4.2. Potential between two charged particles distance  $r$  apart. When the ions are not screened, (b), they repel each other and the barrier is sometimes sufficient for a colloidal solution to survive tens of years or even a century. By adding a salt to the solution the screening changes, (a), and the colloid is then no longer metastable. Aggregation will then occur.

existence today. The addition of a salt to the liquid introduces free ions oppositely charged to the particles in suspension, and partially or totally screens the repulsive interaction. When  $\epsilon$  is of the order of, or is less than,  $kT$ , aggregation begins and the solution becomes unstable. The aggregates increase in size and start to diffuse light by the time they measure about a micron across. This effect is signalled by the appearance of an opalescence.

The cluster size distribution is very sensitive to the height of the potential barrier. Aggregates are formed in the following manner: so long as the colloidal particles are distant from each other, they diffuse in a Brownian way, since the screening suppresses their Coulomb repulsion (i.e., at large distances they do not interact).

When the screening is total, two particles approaching each other at a distance close enough for a strong van der Waals attraction to occur between them, will irreversibly stick to one another. The doublet thus formed continues to diffuse in the liquid where it meets other particles or doublets which then combine to create a larger cluster, and so on. Aggregation occurs rapidly in this

situation, each encounter between clusters causing them to stick to each other first time.

If the screening is not total and the potential barrier,  $\epsilon$ , is a little higher than  $kT$ , many attempts must be made before sticking takes place (the probability of sticking is given by Arrhénius' law). These unsuccessful attempts profoundly modify the structure of the aggregates which are in this case much more compact than when the screening is total. The fractal dimension and other geometric and kinetic properties are thus directly related to the mechanics of the aggregation process. In the first case, aggregation is diffusion-limited, while in the second it is the reaction (crossing the potential barrier) which limits aggregation (see Table IV above). In the latter case, aggregation is therefore much slower.

Weitz's experiments on aggregation in gold colloids are among the most accurate determinations of the scaling properties of irreversible growth processes. To carry out these determinations he used transmission electron micrographs. Gold colloids are especially well suited to the use of these techniques, since they produce large, widely contrasting aggregates. The gold particles are obtained by reducing  $\text{Na}(\text{AuCl}_4)$ . The sol thus produced is stable and contains particles around 14.5 nm in diameter, which are very uniform in size. Aggregation begins when pyridine is added, which has the effect of displacing the surface charges of the particles. The aggregates obtained at the end of this process are about a micron across.

The micrograph shown in Fig. 3.4.3(a) indicates that this is a diffusion-limited cluster-cluster process; the aggregates are all about the same size. In an aqueous solution conditions for aggregation are such that the aggregates form in less than a minute. This shows that they are sticking to each other at the first encounter. The mass varies as a function of the radius as follows:

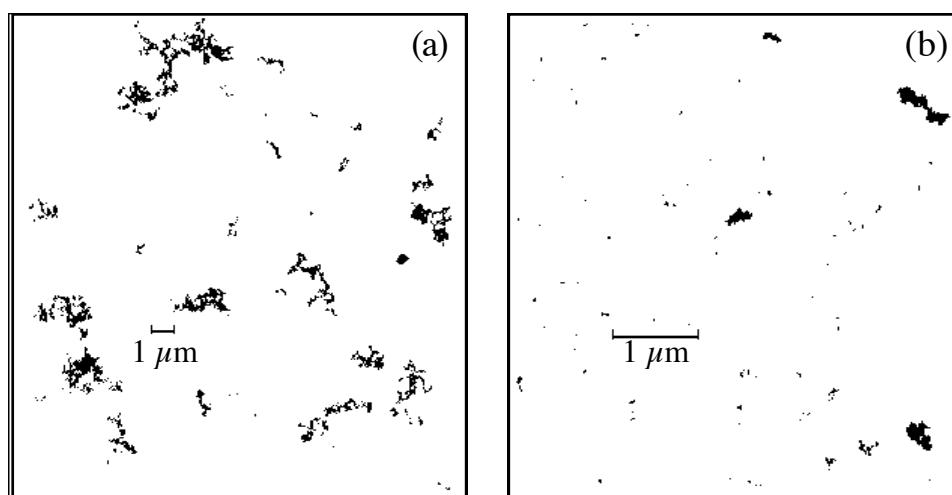


Fig 3.4.3. Photographs of gold colloids taken by Weitz using an electron microscope where (a) aggregation is fast (strong screening) and (b) aggregation is slow (weak screening) (Weitz and Lin 1986; see Matsushita in Avnir, 1989).

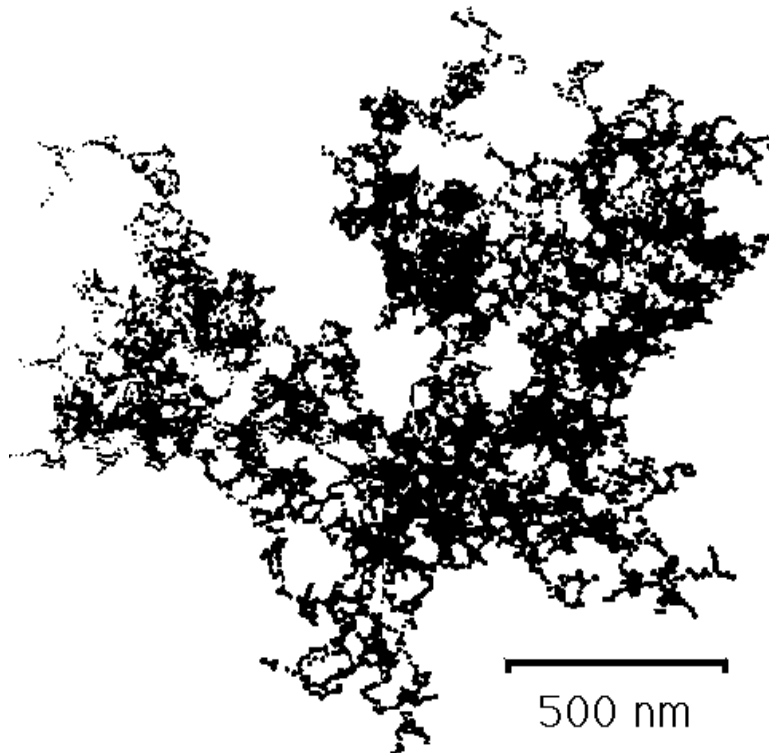
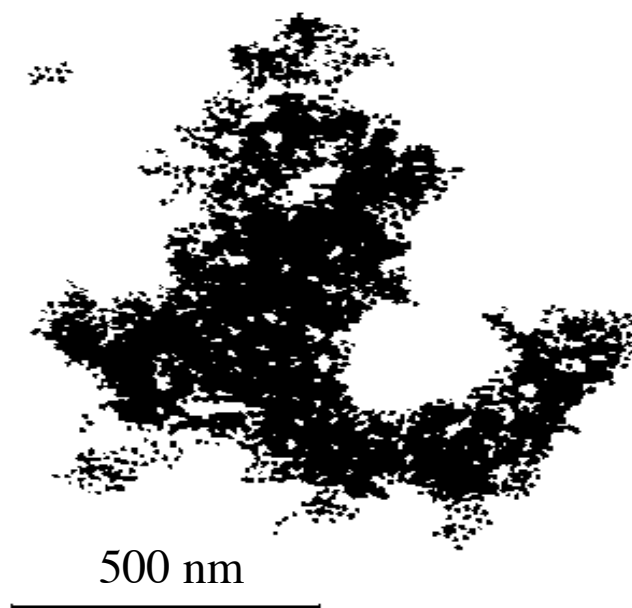


Fig. 3.4.4. Image from a transmission electron microscope of a gold colloid aggregate produced under conditions allowing fast, or, diffusion-limited, aggregation (Weitz and Oliveria, 1984).

$$M \propto R^D, \text{ where } D \cong 1.78,$$

the sign of a fractal structure. The aggregate is self-similar and so has no scale lengths other than the particle and cluster sizes at any given moment. Figure 3.4.4 is an image of one of these clusters taken by a transmission electron microscope.

The images shown in Figs. 3.4.3(b) and 3.4.5 are from an experiment carried out by Weitz and Lin, in which the addition of less pyridine to the sol causes the potential barrier to be only *partially screened*. We can see that the aggregates here are more compact. This variety of cluster–cluster aggregation is reaction-limited (RLCA — reaction-limited cluster aggregation). The dimension is found to be  $D \cong 2.05$  (Weitz et al., 1985). Note that, as this dimension is greater than 2, it cannot be obtained numerically from the two-dimensional image generated by projecting the cluster onto a plane, because such an image would be densely filled by particles (in Fig. 3.4.5, the holes in the central region of the cluster are of relatively uniform size, indicating a non-fractal projection, hence a dimension  $D \geq 2$ ).



*Fig. 3.4.5. Image from a transmission electron microscope of a gold colloid aggregate produced under conditions of slow, or, reaction-limited, aggregation (Weitz et al., 1985).*

Fortunately, there are other methods of displaying the fractal nature of colloidal aggregates when they are of dimension  $D > 2$ . One of these, employed experimentally by Clément and Baudet (Fig. 3.3.7), consists in examining plane sections (whose dimension is  $D - 1$ ). Of course, this method would not work here due to the aggregates' fragility and their small size. Other methods employ techniques such as nuclear magnetic relaxation (Chachaty et al., 1991), but one of the most recent techniques relies on small angle scattering.

#### ***The use of scattering at small angles to determine fractal dimensions***

Experiments involving the scattering of light, X rays, or neutrons are very well suited to investigate the fractal geometric characteristics of those samples whose two-dimensional images cannot be digitalized. Currently they are being used to study aggregates as well as samples of gels (especially silica aerogels).

The scattering intensity depends principally on variations in the density. Thus, for materials displaying a fractal structure, the intensity will depend on the nature of that structure. Pfeifer has proposed that three broad classes of structure should be distinguished: mass fractals, pore fractals, and surface fractals (Fig. 3.4.6). As regards wave scattering, the difference between mass fractals and pore fractals is relatively slight. This is because a mass fractal becomes a pore fractal, and vice versa, simply by interchanging the regions of matter and empty space.

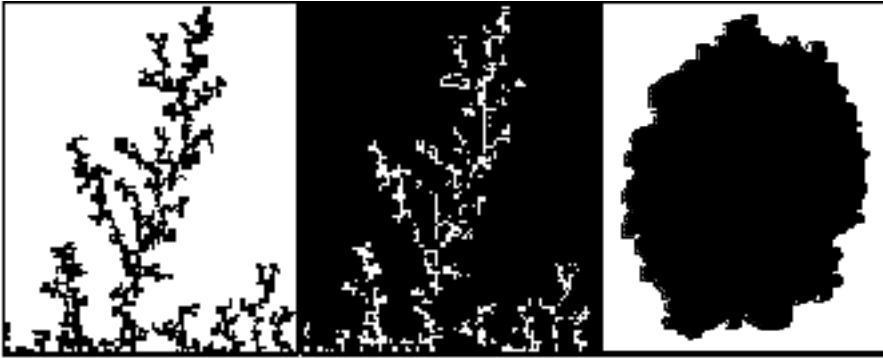


Fig.3.4.6. From left to right a mass fractal, a pore fractal, and a surface fractal. The matter is shown in black or gray, the empty regions in white. The surface fractal (an Eden cluster) is dense in its interior ( $D = d$ ). A surface fractal very often has a self-affine structure.

The scattering experiment is set up as shown in Fig. 3.4.7. The use of light, X rays and neutrons allows the sample to be explored at wavelengths ranging from  $1 \text{ \AA}$  to  $1 \mu\text{m}$ . When experiments are carried out on aggregates they are generally found to be mass fractals.

The intensity of radiation scattered at small angles ( $Q$  small) by a mass fractal as a function of the fluctuation  $Q$  of the wave vector is given by

$$I \propto Q^{-D}, \quad (3.4-3)$$

where  $Q = 4\pi \lambda^{-1} \sin(\theta/2)$ . The fluctuations in the wave vector are related to the fluctuations in the local density; a lack of uniformity in the sample causes the wave to scatter.<sup>13</sup> Thus, the density variation in a fractal structure yields

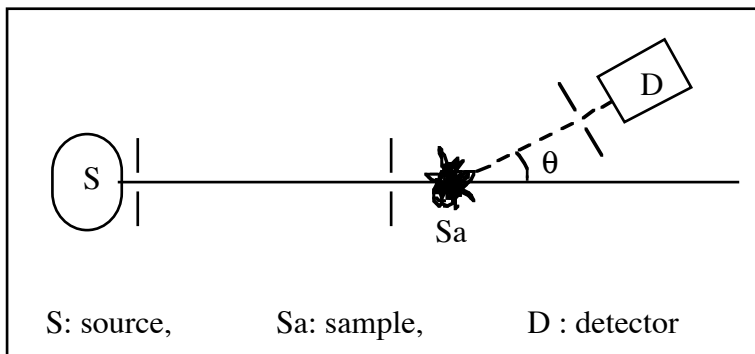


Fig. 3.4.7. Schematic diagram of the measurement of small angle scattering. The source emits radiation of wavelength  $\lambda$  (visible light, X rays, or neutrons). Experimentally  $\theta$  is varied, while  $\lambda$  is held constant.

Eq. (3.4-3). This relation is derived by taking the Fourier transform of the

<sup>13</sup> The tiny isolated (approximately spherical) particles give a law in  $Q^{-4}$ , for values of  $Q$  of the order of the reciprocal of the particle size; this is Porod's law.

density–density correlation function  $g(r)$ . More precisely,

$$I(Q) = A \int_0^{\infty} g(r) \frac{\sin Qr}{Qr} r^2 dr \quad (3.4-4)$$

where  $Q$  is the wave vector length.

The relation in  $Q^{-D}$  is valid as long as  $1/Q$  remains within a domain ranging from the size of a particle to the cluster radius (to be exact its radius of gyration or correlation length). It tells us, therefore, not only about the fractal dimension of the scattering object, but also about the extent of the fractal domain.

This small angle scattering technique was the one used by Weitz and Oliveria to determine the fractal dimensions of the clusters shown in Figs. 3.4.4 and 3.4.5. They found dimension values,  $D = 1.77 \pm 0.05$  for diffusion-limited aggregation, and  $D = 2.05 \pm 0.05$  for reaction-limited aggregation. Other experimenters have obtained similar results in agreement with the results produced by numerical simulations (which give 1.75 and 2.11, respectively; see table IV in Sec. 3.4.1).

This technique has also been used on silica aggregates (see, e.g., P.W. Schmidt in Avnir, 1989). Silica and alumino-silicate aerogels are the most suitable materials for this type of work (Vacher et al. 1988; Chaput et al., 1990). Aerogels have a mean density ranging from  $5 \text{ kg/m}^3$  to  $250 \text{ kg/m}^3$ , while the particles that make them up have a density close to  $2100 \text{ kg/m}^3$ . Since the mean density of a fractal tends to zero as its size increases, the lighter the aerogels are, the larger is the range of their fractal region. Furthermore, aerosols also have remarkable thermal insulating properties. We shall meet them again in Chap. 5 when we study transport and vibration modes in fractal structures.

Fig. 3.4.8 shows the variation of  $I(Q)$  for several different aerogels densities, and demonstrates the progressive appearance of increasingly extended fractal structures as the mean density decreases. The curves display two changes of régime: one when  $Q \cong 0.07 \text{ \AA}^{-1}$ , corresponding to scattering off the constituent particles of the material, producing, for large  $Q$ , a Porod régime; the other for values of  $Q$  between  $10^{-2}$  and  $10^{-3}$ , corresponding to the correlation length of the fractal régime (and so directly related to the density).

In general, for a fractal whose volume is of dimension  $D$  and which is bounded by a surface of dimension  $D_s$ , it can be shown that the intensity takes the form

$$I \propto Q^{-2D+D_s} \quad \text{with} \quad d-1 < D_s \leq D < d. \quad (3.4-5)$$

From this expression we can recover the result for scattering off a mass fractal, as this corresponds to  $D = D_s$ , as well as for scattering off a nonfractal object for which  $D = 3$  and  $D_s = 2$  (Porod's law).

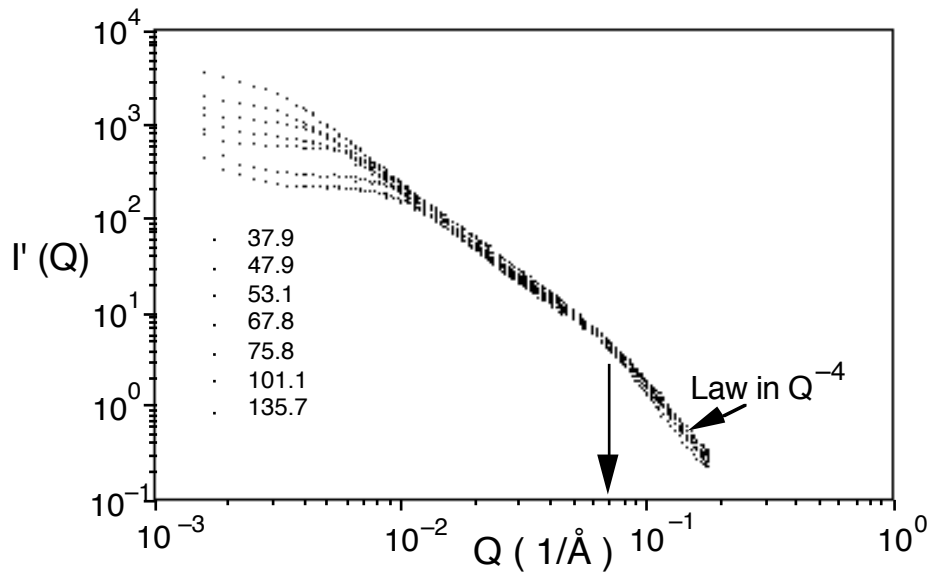


Fig. 3.4.8. Graphs of small angle neutron scattering exhibiting the self-similarity of samples of varying density. The densities,  $\rho$ , are shown in the figure in  $\text{kg/m}^3$  in the same order as the graphs. The intensity has been normalized:  $I'(Q) = I(Q)/\rho$ . This reveals the remarkable way in which the graphs overlap within the fractal region. The left-hand limit of the fractal region occurs where the slope changes abruptly (from 100 to 400 Å). The arrow corresponds to the size of the constituent particles, around 14 Å (Chaput et al., 1990).

For surface fractals of dimension 3, we find

$$I \propto Q^{-6+D_s}, \quad \text{with } 2 < D_s < 3. \quad (3.4-6)$$

Surface fractals are found in a number of different growth processes, both ballistic and reaction-limited (cf. Table IV in Sec. 3.4.1, and Chap. 4 on growth models). In particular, scattering experiments have been carried out on soots produced by aggregation of silica and on colloids. In this way, the fractal dimensions of their rough surfaces can, in principle, be determined (see Schaefer, 1988). Interpretation of these results is rather difficult due to the presence of large regions where the régime is changing (i.e., passing from a surface fractal régime to a mass fractal or Porod régime).

We should also mention that neutron scattering techniques have displayed fractal structures occurring in natural rocks. Experiments on many sandstones and clay schists have shown their behavior to be governed by Eq. (3.4-6), and their dimension  $D_s$  up to 500 Å to be between 2 and 3 (cf. the article by Po-zen Wong, 1988).

### 3.4.3 Macroscopic aggregation

There are other aggregation processes which are more readily observable. For instance, when particles are held in suspension in a liquid, they may reach up to a millimeter in size (unlike colloid and aerosol particles which may be much smaller than a micron). When the particle interactions are negligible (in

particular, in relation to the forces generated by the liquid's motion), aggregation does not take place and the main problem, which is extremely important for studying lubricants, is to try to understand the various characteristics (viscosity, etc.) of the heterogeneous fluid. When the particle interactions are too large to be ignored, aggregation also occurs, on top of which are superimposed hydrodynamic effects due to the motion of the carrier liquid (shearing, etc.).

Here we mention a couple of experiments involving two-dimensional macroscopic aggregation, one performed at the Ecole de Physique et Chimie in Paris, the other at Marseille. In the experiment carried out by Allain and Jouhier (1983), balls of wax of diameter 1.8 mm were placed on the surface of a tank of water. Due to the surface depression caused by each ball, there is a short range (of a few millimeters) attraction between them (the mattress effect). The experiment commences by agitating the water to disperse the balls over its surface. As soon as the agitation dies down, aggregation can be observed and two-dimensional structures of dimension  $D \cong 1.7$  are produced, compatible with a cluster-cluster DLA model (DLCA). In the experiment carried out by Camoin and Blanc (Camoin, 1985), aggregation was observed under shearing: when there is no interaction between the microspheres,<sup>14</sup> the clusters generated have the structure of a "stirred" percolation cluster, producing nearly mean-field behavior; in the presence of an attractive interaction, there is a critical shearing rate above which the hydrodynamic effects start to dominate the capillary effects. Thus, in the presence of strong shearing, the clusters obtained are compact.

All the processes that we have just described are cluster aggregation processes. To observe clusters growing via particle-cluster aggregation, we must have (fixed) nucleation centers distributed sufficiently far apart so that the forming clusters do not influence each other. Even here, growth may be diffusion-limited, reaction-limited or ballistic. There now follow several examples of aggregation which are more or less adequately modeled by either a diffusion-limited particle-cluster process, a process equivalent to DLA (see diffusion-limited aggregation in Chap. 4) or a ballistic particle-cluster process, as in the case of sedimentation.

#### 3.4.4 Layers deposited by sputtering

Under certain conditions, DLA-type structures may be observed in layers deposited by sputtering. The photograph in Fig. 3.4.9 shows such a structure. Elam and his collaborators (1985) produced it by depositing a thin layer of NbGe<sub>2</sub> onto a substrate of quartz. The NbGe<sub>2</sub> atoms adsorbed on the

---

<sup>14</sup> To modify the interaction between spheres a thin layer of viscous liquid (vaseline oil for example) is added to the carrier liquid (which is pure or salt water). When the thickness of this layer is of the order of the diameter of the particles, the interaction between them becomes negligible.

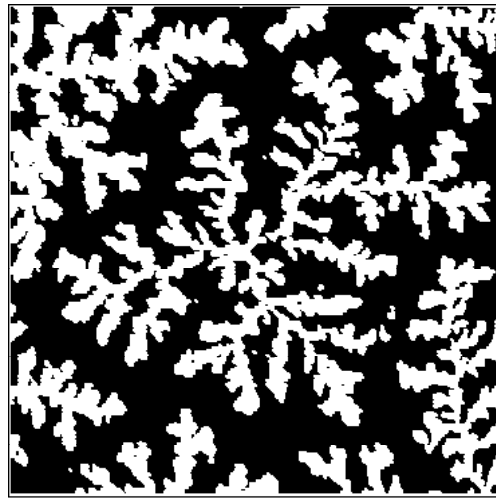


Fig. 3.4.9. Example of a structure obtained by depositing  $\text{NbGe}_2$  onto a substrate of quartz (from Elam et al., 1985).

quartz diffuse until the moment they start sticking to one of the clusters growing from a nucleation center. A cluster may be thought of here as possessing a double structure: it is made up of a skeleton obtained by reducing each branch to a simple line, which is then increasingly thickened towards the tips. In this way, the authors found a fractal dimension of about 1.88 for the  $\text{NbGe}_2$  structures, but a dimension  $D \cong 1.7$  for the skeleton, a value which agrees with the particle–cluster aggregation model. The clusters do not aggregate among themselves, but even so, the nucleation centers are possibly not far enough apart for all mutual influence to be ignored during the final stage of growth. We are a long way from having a clear picture of this type of growth phenomenon.

### 3.4.5 Aggregation in a weak field

When an external systematic force (i.e., one other than a particle interaction) is applied to the particles, there is said to be aggregation in a field. The aggregates obtained, however, vary greatly depending on the type of force acting on the system. It may be a truly external force (that is, not involved in the growth process) such as gravity or the driving force due to the carrier fluid. The following paragraphs provide some examples.

#### *Sedimentation*

The particles form aggregates under the action of gravity. Their motion is thus essentially ballistic. The less the particles diffuse on the surface of the aggregate, the looser the structures formed. We shall describe them in greater detail in Sec. 4.3 on rough surfaces.

### Filtration

The particles carried by a moving fluid congregate around the holes of a filter (as when dust aggregates in the openings of a ventilator). Here again the ballistic aspect dominates.

But in other situations such as electrodeposition, dielectric breakdown, or the rapid injection of one fluid into another more viscous one—phenomena which have many characteristics in common—the (electric or hydrodynamic) force may vary with the growth of the cluster itself. We shall see in Sec. 4.2 that the model common to this method of growth is, to a first approximation, diffusion-limited aggregation (DLA). The structures obtained are also fairly similar to those produced by Elam et al. (Fig. 3.4.9) where no external field is present.

### Electrolytic deposits

These are obtained by depositing metallic atoms onto the cathode during electrolysis of a metallic salt (Fig. 3.4.10). These extremely fragile structures are even more ramified when a dilute solution and a weak current are used.

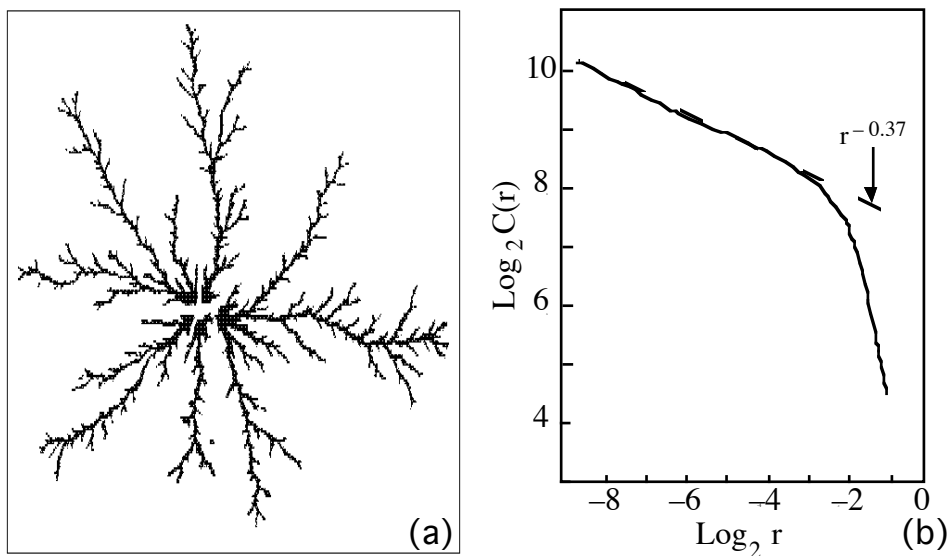


Fig. 3.4.10. (a) Electrolytic growth of metallic zinc in a thin layer of electrolyte and (b) its correlation function giving a dimension  $D = 2 - 0.37$  (Matsushita et al., 1984).

### Dielectric breakdown

Similar structures are observed when an electric field is applied between a central electrode and a circular electrode separated by an insulator (with the same geometry as in the electric deposition experiment) (Niemeyer et al., 1984). Strictly speaking, there are no particles being displaced but only

molecules being polarized until the breakdown threshold is reached (Fig. 3.4.11).

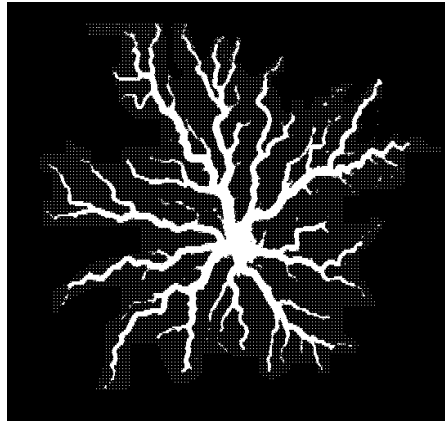


Fig. 3.4.11. Time-integrated photograph of a surface leader discharge on a 2 mm glass plate, placed in gaseous  $SF_6$  at a pressure of 3 atmospheres (Niemeyer et al., 1984).

### **Fluid injection**

In around 1984, Paterson noticed that when a fluid of low viscosity is injected into a radial Hele–Shaw cell filled with a viscous fluid, structures may be observed whose growth is governed by the DLA model (Paterson, 1984). These structures appear, for instance, when low viscosity fluids are injected so as to displace a very viscous fluid inside a porous medium, as shown in Fig. 3.4.12. This corresponds to the viscous fingering in the phase diagram (Fig. 3.2.11) proposed by Lenormand et al. (1988), which wespoke of earlier. The

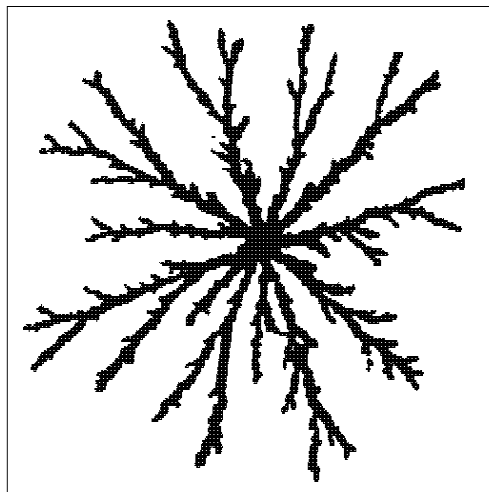


Fig. 3.4.12. Water displacing a polysaccharide solution (scleroglucane) in a radial cell. The viscosity ratio is  $M \cong 1/1500$ ; the rate of flow 20 ml/mn. The Hausdorff dimension measured is  $D_f \cong 1.7 \pm 0.05$  (Daccord et al., 1986).

porous nature of the medium introduces a random aspect which is superimposed on the hydrodynamic process. The more prominent the local randomness, the greater the ramification of the fractal structure.<sup>15</sup> In the images shown in Fig. 3.4.13, the boundary conditions are no longer radial, as was the case in the previous figures. However, the geometric characteristics, such as the fractal dimension and the multifractal structure, are similar.

Daccord and Lenormand (1987) have obtained beautiful structures clearly belonging to the same universality class, that is, diffusion-limited aggregation, by injecting a reactive fluid into a soluble porous medium. This involves the injection of a fluid into a porous medium together with a chemical reaction. In fact, the authors injected water into plaster. The final structure, corresponding to the region of plaster dissolved, is reproduced by injecting Wood's metal (melting point 70°C). One of these three-dimensional structures is shown in the color plates at the end of this book.

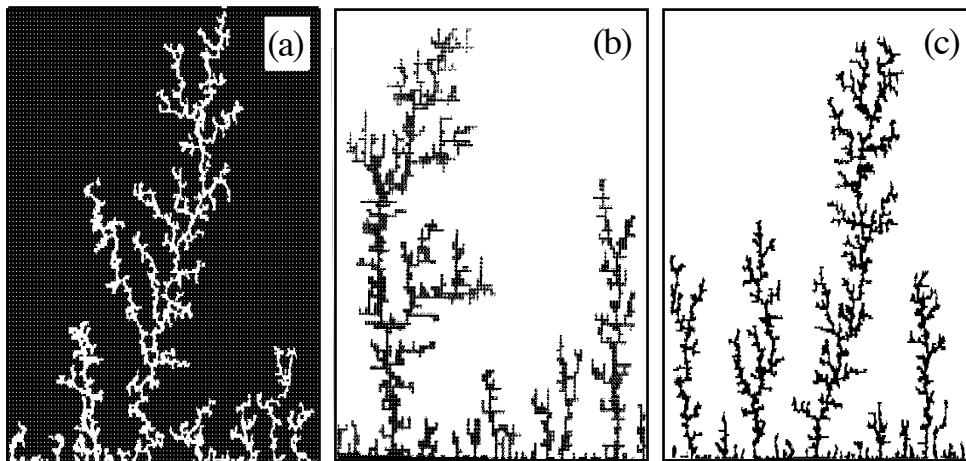


Fig. 3.4.13. Comparison of the structures obtained by (a) injecting a nonwetting fluid in the viscous fingering regime into a porous medium; (b) numerical simulation from the fluid's transport equations in the canals of a porous medium; (c) numerical simulation of diffusion-limited aggregation (Lenormand, 1989).

Let us bring these examples to a close by mentioning the beautiful experiments of Fujikawa and Matsushita (1989) where bacteria colonies, *bacillus subtilis*, are grown on agar plates in a concentration field of nutritional matter. This involves a growth process limited by the diffusion of the nutritional product within the substrate, and generates structures very similar to those that we have just described (the fractal dimension is of the order of  $1.73 \pm 0.02$ ).

In this section we have introduced a variety of new models (Eden, DLA,

<sup>15</sup> The same experiment carried out in a Hele–Shaw cell made from two smooth plates of glass leads to structures with well rounded fingers.

etc.) without describing them in detail. This purely descriptive approach does not allow us to understand how the DLA model relates these diverse phenomena: diffusive aggregation, dielectric breakdown, viscous instability. Chap. 4, which studies growth models, will partially fill this gap. When Witten and Sander put forward the DLA model, which we shall study in that chapter, they intended it to model experiments on iron aerosols carried out by Witten and Forrest. In fact diffusion-limited aggregation does not apply to this situation, nor does it apply, generally speaking, to experiments on colloids or aerosols. Readers should find the film on aggregation processes made by Max Kolb (1986) of great interest.

### 3.5 Polymers and membranes

Polymers and membranes are further examples of structures involving fractal geometries. Here again, the presence of fractal structures can be put down to the large number of configurations that these objects can adopt and to the competition between energy and entropy, which most frequently causes a transition to occur. Linear polymers in solution form a fractal structure ( $D \cong 1.67$ ) at high temperature and a dense structure ( $D = 3$ ) below a certain temperature known as the theta point.

#### 3.5.1 Fractal properties of polymers

Polymers are formed by monomers linking up together in the course of a chemical reaction. This chemical reaction may take place at any of a number of sites on each monomer; the number of sites permitting links is called the *functionality* of the monomer. This process generates ramified structures with irreversible links. If the functionality of all the monomers is 2, the polymer formed is a chain. In other cases ( $f > 2$ ) the polymer is said to be *branched*.

As with percolation, when the lattice of polymerized molecules is sufficiently extended so as to form a very large cluster (*infinite cluster*), we describe it as a *gel*. Gels have an elastic structure (think of the pectine gels used in certain food products), while a lower level of polymerization results in a more or less viscous liquid known as a *sol*.

#### *Linear polymers*

These are produced from bifunctional monomers such as

*polyethylene*:  $\dots - \text{CH}_2 - \text{CH}_2 - \text{CH}_2 \dots$

or *polystyrene*:  $\dots \text{CH}_2 - \underset{\text{C}_6\text{H}_5}{\text{CH}} - \text{CH}_2 - \underset{\text{C}_6\text{H}_5}{\text{CH}} - \text{CH}_2 - \underset{\text{C}_6\text{H}_5}{\text{CH}} - \dots$

Chains are formed when monomers, initially dissolved in a solvent, start to connect. These chains are flexible because they can rotate about their links,



and can be very long. A random walk may be taken as an initial idealized model of a chain, in which each step corresponds to a link and any two successive links can point in arbitrary directions. This type of random walk was described in Sec. 2.2.1. Its fractal dimension is 2 whatever the value of  $d$ . When we study the structure of a polymer formed in this way, i.e., from chains dissolved in a solvent, we find the small angle scattering intensity (Sec. 3.4.2, p. 131) to be of the form  $I \propto Q^{-2}$ .

### *Self-avoiding random walks*

There are, in fact, constraints present for each individual chain and between chains. The interaction  $V(r)$  between two (electrically neutral) monomers has a similar form<sup>16</sup> to the one that exists between two totally screened colloidal particles, represented in Fig. 3.4.2(a). Without entering into details, let us simply say that a useful parameter for describing the effect of this interaction in a solvent at temperature  $T$  is (cf. de Gennes, 1979, p. 56),

$$v = \int \{1 - \exp(-V(r)/kT)\} d^3r. \quad (3.5-1)$$

A *good solvent* ( $v > 0$ ) is one in which the “hard core” monomer interactions are dominant: a polymer in a good solvent should in this case be modeled not by a standard random walk, but by a *self-avoiding random walk*, that is, a random walk that never intersects itself.

The theoretical literature on self-avoiding walks is very large (cf. de Gennes, 1979 and references therein). Here we shall merely describe the very illuminating mean field approach due to Flory (1971). For a linear polymer of mean radius  $R$  in a good solvent, the free energy  $F$  contains a repulsive term  $F_{\text{rep}}$  due to the “hard core” monomer interactions and an entropic term due to the multiplicity of possible configurations. If  $C$  is the local density of the monomers, the repulsive energy is locally proportional to  $C^2$ , so that

$$F_{\text{rep}} \cong kT \int C^2 d^d r = kT v \langle C^2 \rangle R^d \cong kT v \langle C \rangle^2 R^d,$$

where (using a mean field approximation) the mean of the square has been replaced by the square of the mean, and  $d$  is the dimension of the space. The mean density  $\langle C \rangle$  is given by the ratio  $N/R^d$ , of the (fixed) total number of monomers to the volume occupied by the polymer. Hence,

$$\frac{F_{\text{rep}}}{kT} \cong v \frac{N^2}{R^d}. \quad (3.5-2)$$

On the other hand, the entropic part of the free energy  $F_{\text{ent}} = -T S$  (which produces a restoring elastic force) is calculated by determining the number of possible configurations of a random walk of size  $R$  (see Sec. 2.2.1). The size distribution has the form

---

<sup>16</sup> The interaction between monomers a distance  $R$  apart is generally of the Lennard-Jones (12-6) type, that is, it is the difference between a term in  $1/R^{12}$  and a term in  $1/R^6$ .

$$p(R, N) = \frac{A}{N^{d/2}} \exp -B \frac{R^2}{Na^2}$$

and the free entropic energy (proportional to the logarithm of the probability)

$$\frac{F_{\text{ent}}(R)}{kT} \cong \frac{F_{\text{ent}}(0)}{kT} + \left(\frac{R}{R_0}\right)^2. \quad (3.5-3)$$

$R_0$  is the ideal mean radius (in the absence of an interaction), hence  $R_0^2 \propto N$ . The size of a “real” polymer in equilibrium is found by minimizing the total free energy

$$\frac{F - F_0}{kT} \cong \left(\frac{R}{R_0}\right)^2 + \frac{v N^2}{R^d}. \quad (3.5-4)$$

Minimization with respect to  $R$  gives

$$N \propto R^D \quad \text{with} \quad D = \frac{d+2}{3}. \quad (3.5-5)$$

The structure of a *polymer chain in a good solvent is fractal*, its *mean field* fractal dimension is  $D = 4/3$  in  $d = 2$  and  $D = 5/3$  in  $d = 3$ . These values are remarkably accurate (less than 1% from the best numerical values). In two dimensions, the “exact” approach using the conformal invariance gives  $D = 4/3$ .

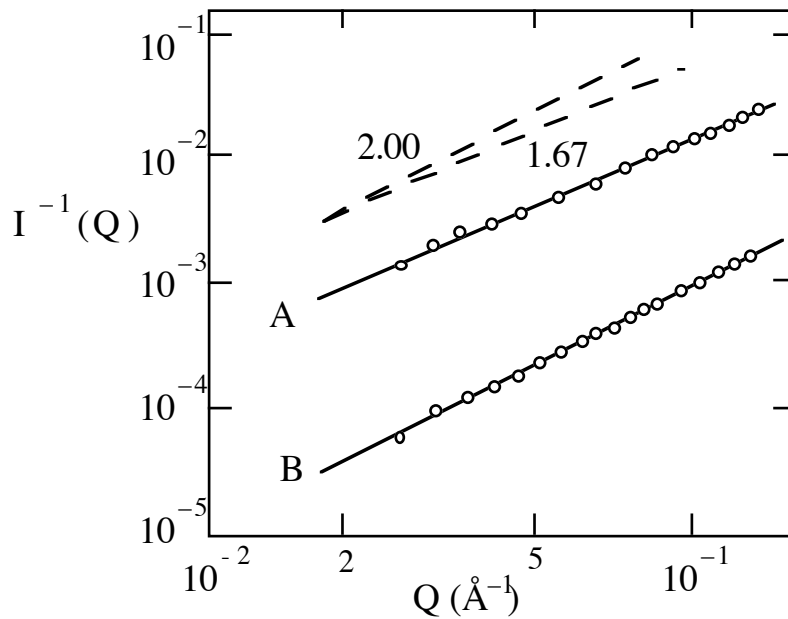


Fig. 3.5.1. Experimental data of small angle neutron scattering off polystyrene chains dissolved in benzene (curve A); the gradient  $5/3$  is shown as a dashed line. In the case of molten polystyrene (curve B), the gradient attained is 2, since screening causes a chain in a molten polymer to be modeled by a random walk (Farnoux's thesis, cf. Daoud and Martin in *Avnir*, 1989).

Experiments with neutron scattering have been carried out on polystyrene

dissolved in benzene. This solvent may be considered as a good solvent, and the scattering intensity is found to follow very closely the relationship  $I(Q) \propto Q^{-D}$  with  $D = 5/3$  (Fig. 3.5.1).

This is so as long as the polymer is dilute enough in the solvent for the interaction between chains to be neglected. If the monomer concentration  $C$  is steadily increased, a concentration  $C^*$  is reached at which the polymers overlap. This concentration is equal to the concentration of monomers in a chain, that is,

$$C^* \cong \frac{N}{R^d} \propto N^{1-d/D} \propto N^{-4/5} \quad (\text{in } d = 3) . \quad (3.5-6)$$

### Scaling laws

As  $C^*$  plays the role of a critical concentration, we should expect the dimensionless ratio  $C/C^*$  to be the relevant parameter in problems involving polymers dissolved in good solvents. Any property dependent on  $N$  and  $C$  may thus be written

$$F(N,C) = F(N,0) f(C/C^*) \quad (3.5-7)$$

or alternatively,

$$F(N,C) = F(N,0) f(CN^{4/5}) .$$

### Polymer chains in a bad solvent

This is how we describe the case where  $v < 0$ , for then the free energy defined by Eq. (3.5-4) no longer possesses a minimum. The series must be expanded to higher order, since the term for the monomer interaction (in  $C^2$ ) is now negative, that is, dominated by the attractive part of the interaction. The term in  $C^3$  (for three bodies) remains positive and  $v$  vanishes at the transition temperature  $T = \Theta$ :

$$\frac{F - F_0}{kT} \cong \frac{R^2}{R_0^2} + \frac{v N^2}{R^d} + \frac{w N^3}{R^{2d}} + \dots \quad (3.5-8)$$

For temperatures below the  $\Theta$  point ( $v < 0$ ), the polymer “collapses” to a dense structure and  $D = d$ . All orders ( $n$ -body interactions) now play a role.

### Polymer chains without a solvent and vulcanization

A plate of spaghetti provides a good picture of a collection of chains at concentration  $C = 1$ , i.e., with no solvent, so long as the temperature is sufficiently low. At ordinary temperatures, thermal agitation must be taken into account—in which case a box full of earthworms would give a more realistic image. This material is soft and stretches irreversibly when pulled. If bridges are now created between the chains (as during vulcanization when sulfur bridges S–S are introduced between polyisoprene chains), a material is formed

which keeps its shape: a *rubber*. Only a small concentration of bridges is required to make an “infinite” cluster of connected chains.

### ***Branched polymers***

Consider a solution of monomers all with the same functionality,  $f$ . If links are formed at all the extremities without any loops being made, then a Bethe tree is produced (see Fig. 3.1.3). The lack of available space is very quickly felt; a Bethe tree with excluded volume cannot be embedded in a finite dimensional space. Consequently, either the polymer contains a large number of *dangling* bonds, or else the polymer restructures itself by closing up at least these bonds.

A “Flory–Stockmayer” approach via a mean field theory, based on a Cayley tree model ( $D = 4$ ) (see the mean field approach to percolation in Sec. 2.4.1), yields

$$N \propto R_0^4.$$

At the start of the 1980s, Isaacson, Lubenski, and de Gennes performed a calculation taking account of the excluded volume condition in a form similar to the case of linear polymers. The branching polymer is assumed to be in thermal equilibrium in a solvent in which it is sufficiently diluted. By minimizing the total free energy as shown above with respect to  $R$ , it is found that

$$\boxed{D = \frac{2(d+2)}{5} \quad (D = 2 \text{ when } d = 3)} . \quad (3.5-9)$$

In fact, this calculation only corresponds to the fractal dimension if the system is restricted to a single cluster and to distances less than its size. In practice, when polymerization takes place, the medium becomes polydisperse, and this polydispersity must be taken into account when calculating the effective fractal dimension of the medium.

With a cluster distribution of the form  $n_s = s^{-\tau}$  at the percolation threshold, the fractal dimension is found to be

$$\boxed{D_{\text{eff}} = D(3 - \tau)} . \quad (3.5-10)$$

so by taking  $\tau \cong 2.2$ , we have, for  $d = 3$ ,  $D_{\text{eff}} \cong 1.6$ .

These two values, 2 for a monodisperse medium and 1.6 for a polydisperse medium, have been well verified experimentally.

It would also be interesting to investigate the structure of *molten polymers*, since then no solvent is present, bringing about a partial screening between the polymers, and so to an increase in the fractal dimension. The interested reader should consult specialist books and articles (de Gennes, 1979; Daoud and Martin in Avnir, 1989; etc.).

### ***Gels***

We must distinguish here between physical gels and chemical gels. With

*physical gels*, we are dealing with polymers in fairly long chains in the presence of a “bridging agent” (such as  $\text{Ca}^{++}$ ), unless they roll up in a spiral (Fig. 3.5.2). Bridges start to form between the chains at a concentration level determined by the temperature (the energy needed for these bridges to form is usually quite low). At high temperatures, there are few links and the polymer is liquid. At low temperatures, the system is frozen by the large number of links present. Between these two extremes, there is a gelation temperature at which the mean number of links present insures the existence of an infinite cluster. In all these cases the system can be maintained in a liquid or solid state by adjusting the temperature. Gelatine is a physical gel which melts at  $60^\circ\text{C}$ .

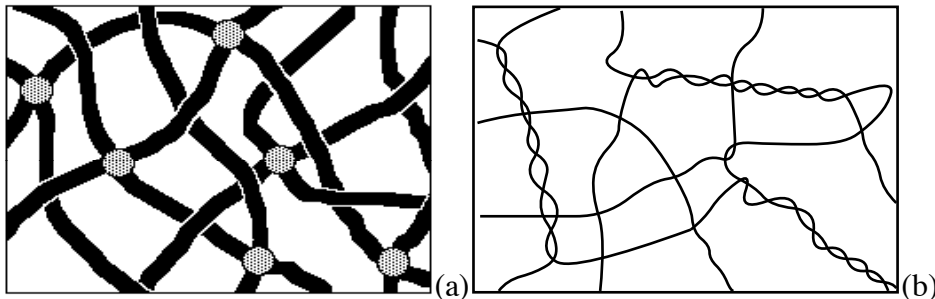


Fig. 3.5.2. Formation of a physical gel. Linear polymers may be bonded to each other by ionic bridges or roll up into a helix. Bridges may be formed in sufficient concentration to produce an infinite cluster and thus to form a gel. The temperature controls the opening of these bridges whose formation barrier is fairly low.

With *chemical gels*, the structure is constructed by chemical bonding between the constituents (epoxy resins and glues are examples). For a long time, the system does not reach equilibrium, because the aggregation involved is either of the diffusion or the reaction-limited cluster–cluster type (and is assumed to be relatively monodisperse). Because of their fractal structure, as the polymerized clusters grow, their mean concentration decreases and so they occupy more and more space. The monomer concentration of a cluster of radius  $R$  and mass  $M = R^D$  is  $C = M/R^d$ , while outside the clusters it is nearly zero. When  $C$  has decreased sufficiently and reached the initial concentration  $C_0$ , the clusters end up touching each other [Fig.3.5.3 (b)]. Thus, their mean radius  $R_G$  satisfies

$$C_0 = R_G^{-(d-D)}$$

The aggregation process produces a certain growth rate for the clusters, thereby causing their mean radius  $R(t)$  to depend on the time,  $t$ . Thus, at a particular time,  $t_G$  [ $R(t_G) = R_G$ ], called the *gelation time*, an infinite cluster appears.

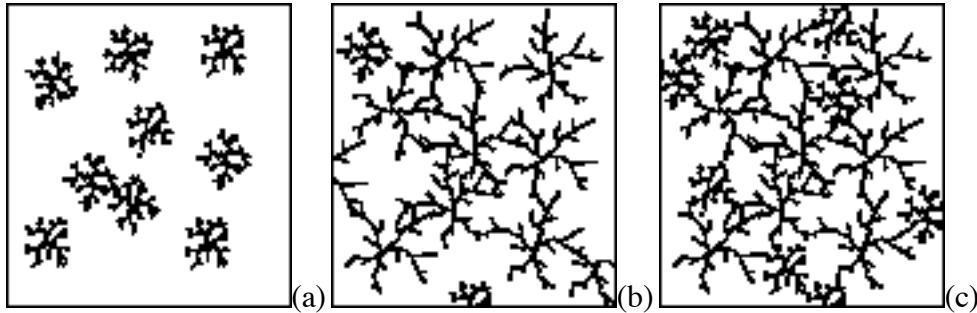


Fig. 3.5.3. Formation of a chemical gel: as long as the monomers are sufficiently dilute the polymerized clusters remain separate (a). At a time  $t_G$ , gelation occurs (b). After a longer time, there may be restructuration within the gel and densification (c). Polydispersity plays an important role in these processes.

The dynamics are, in fact, governed by the diffusion coefficient of each type of cluster. The larger their volume, the slower they diffuse. It is reasonable to assume a power law for these diffusion coefficients,  $\mathcal{D}(M)$ , a law which agrees with experimental results. Thus (Kolb and Herrmann, 1987),

$$\mathcal{D}(M) = M^\gamma \text{ with } \gamma < 0.$$

The growth rate depends essentially on  $\gamma$ . The temperature also plays an important role in these growth rates.

Flory's mean-field treatment of the successive branching of monomers using Cayley trees as models, although it gives perfect results for gels, ignores any loops and leads to steric constraints making it impossible for an infinite Cayley tree to be constructed in three-dimensional space. Observed deviations from this model led de Gennes and Stauffer in 1976 (see de Gennes, 1979, p.137) to propose a percolation approach to the case when no solvents are present. If a solvent is present, then, at the moment of gelation, the cluster-cluster process can no longer be diffusion-limited, as the clusters have already penetrated each other. The idea is that links form randomly between the clusters to produce a network similar to a percolation network. The number of these bonds continues to grow in time, in other words, the percolation threshold is exceeded (for more details see Joughier et al., in Deutscher, Zallen, and Adler 1983, Chap. 8).

The passage from a sol (polymer solution) to a gel is easily observed due to alterations in the mechanical properties of the medium. At the moment the gel is formed, the viscosity of the sol increases and diverges, while from this point on the elasticity, which was nonexistent, begins to increase (see Sec. 5.2.4).

### 3.5.2 Fractal properties of membranes

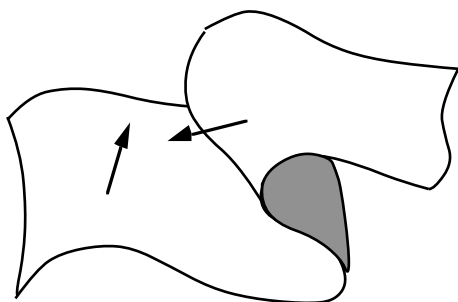
Membranes are structures that play a crucial role in many areas of physics, chemistry, and biology. They are also conceptually very interesting because of

their two-dimensional geometry ( $d_T = 2$ ). Continuing in the same vein, we shall only examine those structural aspects of membranes that lead to fractal geometries. Depending on their local molecular constitution, membranes may present very different structures. On the one hand, there are fluid membranes whose constituent molecules diffuse easily through the heart of the membrane, and on the other, there are solid membranes obtained by polymerization with unbreakable molecular bonds.

### **Fluid membranes**

Amphiphilic molecules are those which possess a hydrophilic (polar) head, along with one or more hydrophobic chains. These molecules readily situate themselves at the interface of two immiscible fluids such as oil and water; they are the surfactants used to make emulsions. They also commonly occur in a two-layered configuration in which the hydrophobic chains pair up. This is how the membranes of living cells are formed, with the hydrophilic heads on the outside in contact with the water of the cells. These membranes fluctuate thermally and, unlike solid membranes, have no resistance to tearing. Locally they can dilate like an elastic membrane.

A correlation length associated with these fluctuations can be defined. To do this we take the mean value of the scalar product of two unit normal vectors at two surface points at distance  $r$  apart. A plane surface corresponds to an infinite correlation length. The fluctuations cause the membrane to crumple and so, in principle, as the temperature increases we should expect a *crumpling transition*. Baumgärtner and Ho (1990) have recently carried out numerical



simulations of crumpling in fluid vesicles.<sup>17</sup> They found that the radius of gyration was related to the number of surface monomers by a power law of the form

$$N \propto R^D \quad \text{with} \quad D \cong 2.5 . \quad (3.5-11)$$

If we think of the crumpled fluid membrane as a self-avoiding random surface, this is not dissimilar to the external surface of a diffusion front as described in Sec. 3.3.1, whose fractal dimension was also close to 2.5.

---

<sup>17</sup> The calculations were carried out on vesicles rather than open membranes so as to avoid problems relating to the free boundaries.

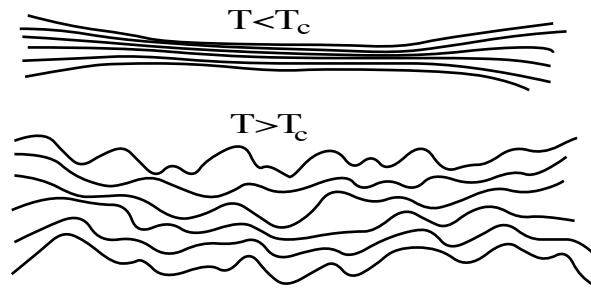


Fig. 3.5.4. Uncoupling transition in a pile of fluid membranes.

In addition, in a stack of membranes it is possible to observe an *uncoupling transition*. Between two membranes there exists an attractive van der Waals force which produces an interaction potential of the type shown in Fig. 3.4.2 (a). At low temperatures the membranes pile up in almost parallel layers. Above a certain critical temperature, the membranes separate (repulsive forces of entropic origin) due to the appearance of fluctuations in their geometries (Fig. 3.5.4). The uneven nature of this geometry does not appear to have been studied in detail.

### **Solid membranes**

A solid or polymerized membrane is a surface which preserves the connectivity between each pair of points on its surface. An example of this is a surface composed of a set of interconnected particles (monomers) in a two-dimensional lattice. The scaling properties of such a surface depend neither on the structure of the lattice (triangular, square, etc.), nor on the precise nature of the short range particle interaction, but only on the fact that the bonds between the particles cannot be broken.

A crumpled piece of paper is a simple example of a solid membrane. Polymerized membranes can also be made from monomers interconnected along liquid–gas, liquid–liquid, or solid–gas interfaces. An example of this is poly(methyl-methacrylate) extracted from the surface of sodium montmorillonite clays. Polymerized membranes have also been obtained by copolymerization of lipidic bilayers.

In two dimensions, the analogues of solid membranes are the self-avoiding chains (polymerized chains moving along an interface) described in the previous paragraph. We have seen that they undergo a transition at the  $\Theta$ -point.

In general, solid membranes involve a repulsive attraction between monomers, which tends to flatten them. Thus, they undergo a phase transition due to the competition between the forces tending to flatten the membrane (simulated by a coupling,  $J$ , between the normals at neighboring regions) and the entropy tending to crumple the surface. Fig. 3.5.5 shows four equilibrium configurations of a solid membrane for various values of  $\kappa = J/kT$ . The phase transition between the flat and crumpled phases occurs at a value close to  $\kappa = 0.5$ .

The radius of gyration,  $R_g$ , of a membrane without excluded volume (no hard core interaction between monomers) in its crumpled phase, varies as  $(\log R)^{1/2}$ , where  $R$  is the linear size of the flat membrane. When the excluded volume interactions are present, the radius of gyration grows as  $R^{\nu_t}$ , where  $\nu_t \cong 0.8$ . You can easily check this exponent 0.8 by crumpling squares of paper with different length sides  $R$ . The crumpled phase is fractal and the mass–radius relation gives

$$D = \frac{d-1}{\nu_t} \cong 2.5 \quad \text{in } d=3 \quad . \quad (3.5-12)$$

Just as with linear polymers, we could make a mean-field calculation here by adopting the Flory approach; the expression obtained generalizes the calculation made for chains and we find

$$D^{\text{Flory}} = \frac{d+2}{d_T+2} d_T \quad . \quad (3.5-13)$$

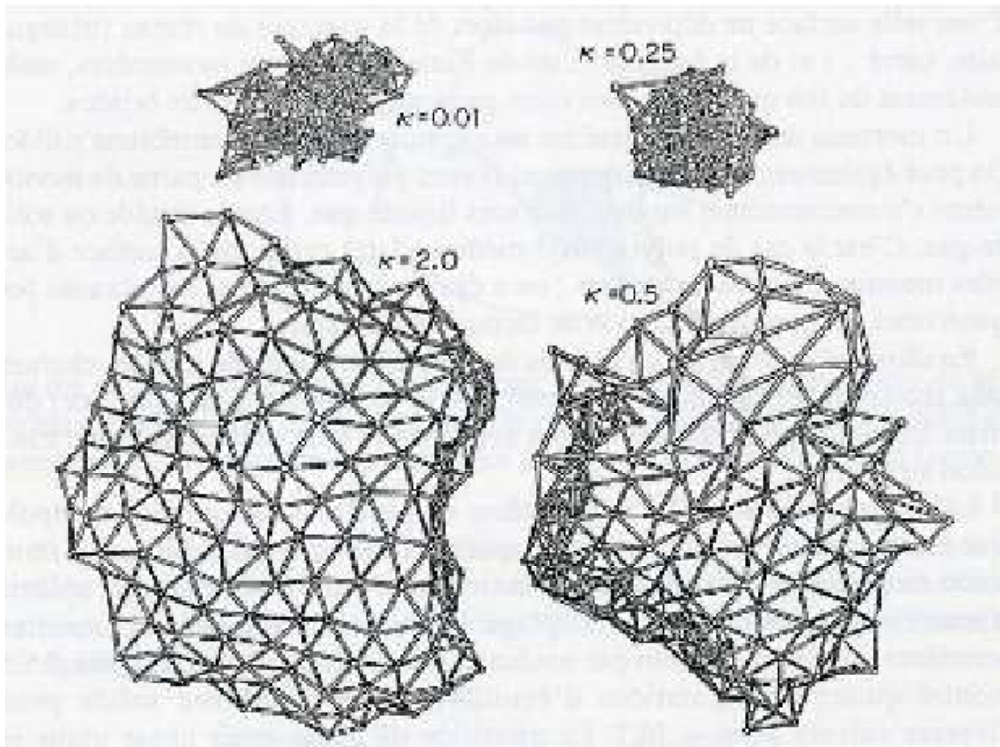


Fig. 3.5.5. Equilibrium configurations of a hexagonal membrane composed of small triangular regions. They correspond to four different values of the reduced interaction,  $\kappa$ , between the normals at neighboring regions.  $\kappa = 0.01$  and  $\kappa = 0.25$  correspond to the crumpled phase,  $\kappa = 0.5$  is close to the transition, and  $\kappa = 2.0$  corresponds to the flat phase (Kantor, 1989).

$d_T$  is the topological dimension of the membrane or chain. For a membrane,  $D^{\text{Flory}}$  is exactly 2.5.